Article

A rationally designed 2C inhibitor prevents enterovirus D68-infected mice from developing paralysis

Check for updates

Kan Li [1,8], Michael J. Rudy[2,8], Yanmei Hu[1,8], Haozhou Tan[1,8], George Lambrinidis[3], Xiangmeng Wu[4], Kyriakos Georgiou[3], Bin Tan [1], Joshua Frost [2], Courtney Wilson[2], Penny Clarke[2], Antonios Kolocouris [3], Qing-yu Zhang[4], Kenneth L. Tyler [2,5,6,7] ✉ & Jun Wang [1] ✉

Enterovirus D68 (EV-D68) is a respiratory virus that often causes mild to moderate respiratory illnesses and, in severe cases, can lead to paralysis and rarely death, mainly in children. There is currently no vaccine or antiviral for EV-D68. Here, we report the rational design of viral 2C inhibitors for treating EV-D68 infection-induced paralysis in a neonatal mouse model. Viral 2C protein is a multi-functional protein vital for viral replication. Structure-based drug design identifies **Jun6504** showing potent and broad-spectrum antiviral activity against multiple strains of EV-D68, EV-A71, and CVB3, as well as favorable in vitro and in vivo pharmacokinetic properties. In a neonatal mouse model of EV-D68 infection, **Jun6504** significantly improves paralysis score and weight gain when administered immediately or 24 hours post-infection. **Jun6504** also reduces viral titers in the spinal cord and the infected quadriceps muscle. Collectively, **Jun6504** represents a promising candidate for further development as an EV-D68 antiviral.

Enterovirus D68 (EV-D68) is one of more than 100 non-polio enteroviruses[1]. EV-D68 was first isolated from children with respiratory illness in California in 1962[2]. People of all ages can be infected, with children being the most susceptible group. Historically, EV-D68 infection generally caused mild to moderate respiratory illnesses; severe cases were rarely reported[3]. However, a large outbreak of EV-D68 in the United States in 2014 gained public attention, with a number of patients showing severe respiratory illness and, in some cases, neurological complications such as acute flaccid myelitis (AFM) with arm or leg weakness[4,5]. Since 2014, a biennial outbreak pattern of EV-D68 infection has occurred, though it was interrupted by the COVID-19 pandemic[6]. EV-D68 cases have resumed after easing COVID-19 precautions in the United States and Europe, but appear to be predominantly respiratory with few reported AFM cases[7,8].

No vaccine or antiviral is available to prevent or treat EV-D68 infection, and treatment is limited to supportive care[9]. Drug repurposing has identified several inhibitors with in vitro antiviral activity in cell culture[9–11]. Representative examples include the viral 3C protease inhibitor rupintrivir, the 2A protease inhibitor telaprevir[12], the VP1 capsid inhibitors pleconaril and pirodavir[13], the 2C inhibitors guanidine[14], fluoxetine[15–17] and dibucaine[18,19], the 3D polymerase inhibitor ribavirin, and the host-targeting antiviral enviroxime[20].

[1]Department of Medicinal Chemistry, Ernest Mario School of Pharmacy, Rutgers, the State University of New Jersey, Piscataway, NJ, USA. [2]Department of Neurology, University of Colorado School of Medicine, Aurora, CO, USA. [3]Laboratory of Medicinal Chemistry, Section of Pharmaceutical Chemistry, Department of Pharmacy, National and Kapodistrian University of Athens, Panepistimiopolis-Zografou, Athens 15771, Greece. [4]Department of Pharmacology and Toxicology, R. Ken Coit College of Pharmacy, The University of Arizona, Tucson, AZ, USA. [5]Department of Immunology & Microbiology, University of Colorado School of Medicine, Aurora, CO, USA. [6]Division of Infectious Disease, Department of Medicine, University of Colorado School of Medicine, Aurora, CO, USA. [7]Neurology Service, Rocky Mountain VA Medical Center, Aurora, CO, USA. [8]These authors contributed equally: Kan Li, Michael J. Rudy, Yanmei Hu, Haozhou Tan. ✉e-mail: ken.tyler@cuanschutz.edu; junwang@pharmacy.rutgers.edu

Fluoxetine did not reduce motor impairment or viral titers in the muscle and spinal cord in an EV-D68 infection neonatal mouse model[21] and failed to improve neurological outcomes in patients with EV-D68-associated AFM[22]. Furthermore, enviroxime, pirodavir, pleconaril, ribavirin, and rupintrivir showed no therapeutic efficacy in the respiratory or neurological disease model following EV-D68 infection in AG129 mice[14]. Only three compounds, including guanidine[14], telaprevir[23], and a pleconaril analog 11526092[24], have shown in vivo antiviral activity in EV-D68 animal infection models[23]. Consequently, designing additional EV-D68 antivirals with in vivo antiviral efficacy in a mouse infection model will significantly advance the field.

2C is a nonstructural viral protein and plays essential roles in the assembly, rearrangement, and replication of viral RNA[25,26]. Mutations in 2C affect viral replication and pathogenesis[27,28]. 2C protein is also highly conserved (Supplementary Fig. 1), and 2C inhibitors have shown broad-spectrum antiviral activities against multiple strains of EV-D68 as well as EV-A71 and coxsackieviruses[9,29,30]. Several 2C inhibitors have been reported, including pyrazolopyridines[31,32], fluoxetine[17], and quinolines[18,19]. However, no 2C inhibitor has shown in vivo antiviral efficacy in animal models of EV-D68 infection except guanidine when tested at high drug doses (100 and 200 mg/kg)[14], and it remains to be validated whether 2C inhibitors can inhibit viral replication and mitigate disease progression in vivo.

In this work, we report the rational design and characterization of **Jun6504**, a 2C inhibitor with demonstrated in vivo antiviral efficacy in a neurological mouse model of EV-D68 infection. Molecular dynamics (MD) simulations suggest that **Jun6504** binds to an allosteric pocket within the viral 2C protein, a binding mode independently confirmed by resistance selection studies and thermal shift assays. **Jun6504** exhibits potent, broad-spectrum antiviral activity against EV-D68, EV-

A71, and CVB3. Additionally, **Jun6504** displays favorable pharmacokinetic (PK) properties, supporting its advancement to efficacy testing in animal models. In a neonatal mouse model of EV-D68 infection, **Jun6504** significantly improves clinical outcomes, including paralysis scores and weight gain, when administered immediately or 24 hours post-infection. Furthermore, **Jun6504** effectively reduces viral titers in the spinal cord and infected quadriceps muscle. Together, these findings establish **Jun6504** as a promising 2C inhibitor with in vivo antiviral activity, further validating 2C as a viable target for antiviral drug development.

Results

Jun571 binds to an allosteric site in 2C

Our previous studies identified a pyrazolopyridine compound, **Jun571**, with potent and broad-spectrum antiviral activity against enteroviruses, including multiple strains of EV-D68[31]. To assist structure-based design, we performed molecular docking calculations and MD simulations to gain insight into the binding mode. The binding interactions between **Jun571** and the EV-D68 2C have been explored using 500-ns-MD simulations with the amber 19 sb force field (ff19sb). For the simulations, the EV-D68 2C protein model was generated based on the X-ray structure of (S)-fluoxetine–CVB3 2C complex (PDB ID 6S3A)[16].

The MD simulations showed that **Jun571** and EV-D68 2C form a stable complex with specific interactions (Fig. 1). Specifically, the terminal tertiary protonated amine in **Jun571** forms ionic hydrogen bonding interactions with Asp160 and Asp183, and a hydrogen bond with Asp186 side chain carboxylate group (Fig. 1a–c); the flexibility of the dimethylaminoethyl group allows the ammonium group to form hydrogen bonding interactions with all three Asp residues surrounding
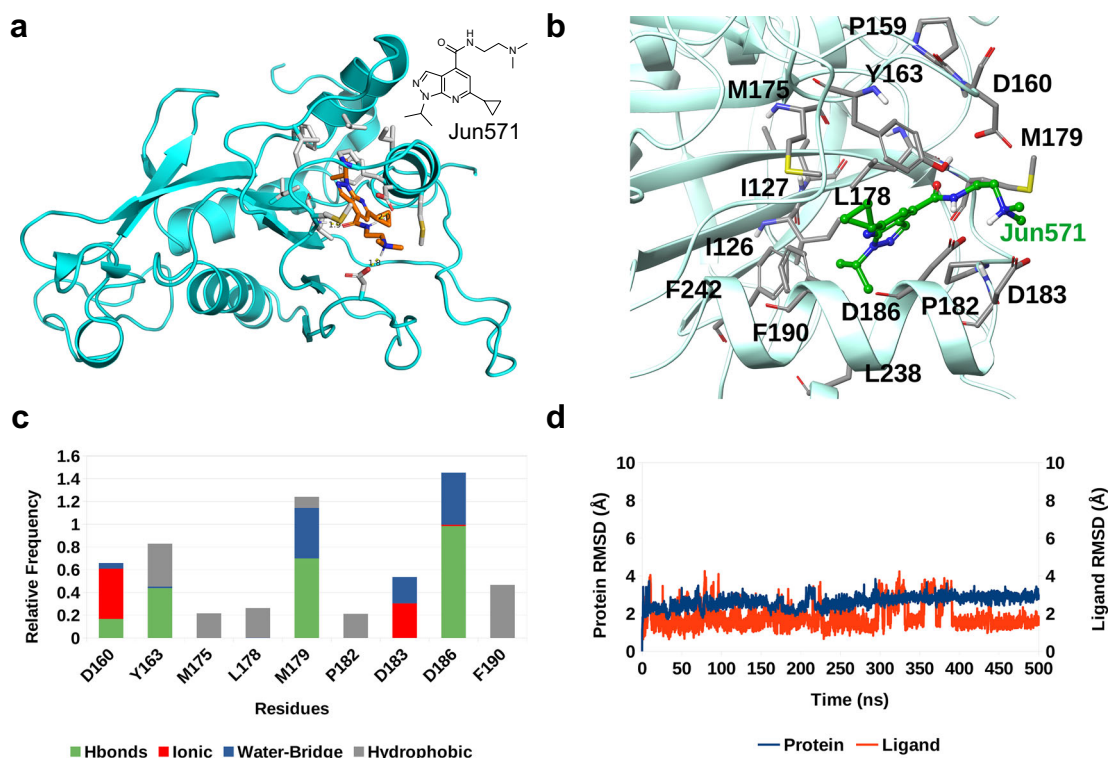
Fig. 1 | Molecular dynamics simulations of Jun571 at the allosteric binding site of EV-D68 2C. a Representative frames from 500-ns-MD simulations of the complexes between **Jun571** and the EV-D68 2C (protein = blue ribbon and gray sticks; ligand's carbons are shown in orange; nitrogen, oxygen, and sulfur are shown in blue and red, and yellow respectively; hydrogen bonding interactions are shown with yellow dashes). **b** Interactions between **Jun571** and the residues at the allosteric site of EV-D68 2C. **c** Stabilizing interactions inside the binding area of 2C with **Jun571**; hydrogen bonding interactions bar is depicted in green, ionic hydrogen bonding interactions in red, water bridges in blue, and lipophilic interactions in gray. **d** RMSD plots of Cα carbons of 2C (blue diagram) and the heavy atoms of the ligand **Jun571** (red diagram).

this group. The amide NH in **Jun571** forms a hydrogen bond with Tyr163 (Fig. 1b, c), and the amide carbonyl in **Jun571** forms another hydrogen bond with Met179 main chain amide NH and a water-mediated hydrogen bond with Asp186 side chain carboxylate group (Fig. 1b, c). The N-isopropyl fits in a hydrophobic pocket consisting of side chains from Ile126, Phe190, Ile227, Leu238, and Phe242, forming significant hydrophobic interaction mainly with Phe190, and the 6-cyclopropyl of the pyrazole forms hydrophobic interactions with M189 while the pyrazole ring is surrounded by hydrophobic amino acid side chains, e.g., Met175, Leu178, Pro182, and Tyr163 (Fig. 1b).

The binding interactions between **Jun571** and the viral 2C proteins of EV-A71 and CVB3 were also explored using 500-ns-MD simulations. For the simulations, the protein models were generated correspondingly based on the X-ray structure of EV-A71 2C (PDB ID 5GQ1)[33] and the structure of (S)-fluoxetine–CVB3 2C complex (PDB ID 6S3A)[16]. **Jun571** similarly forms stable complexes with EV-A71 and CVB3 2C proteins by binding to the allosteric site (Supplementary Fig. 2, 3). **Jun571** forms hydrogen bonds in this site with Asp186 and Cys179 in EV-A71 and CVB3 2C proteins. In addition, **Jun571** is stabilized by van der Waals contacts with Pro159, Leu178, Pro182, Phe190, or Met175, Leu178, Pro182, Phe190, Leu238 in EV-A71 2C and CVB3 2C, respectively. One striking difference is that the terminal tertiary amine in **Jun571** does not form hydrogen bonding interactions with the Asp160 side chain carboxylate in the EV-A71 and CVB3 2C complex structures (Supplementary Fig. 2b–d and Fig. 3b–d), as it did in EV-D68.

To validate that **Jun571** binds to the same site as (S)-fluoxetine in CVB3 2C, we performed a differential scanning fluorimetry (DSF) binding assay. The CVB3 2C-D183V and D186A mutants with mutations located at the proposed drug binding site had reduced binding to **Jun571** compared to WT (Supplementary Fig. 3g), suggesting that **Jun571** binds to the same allosteric site as fluoxetine.

Lead optimization identified multiple candidates with improved mouse liver microsomal stability

Given the potent antiviral activity, high selectivity index, and broad-spectrum antiviral activity of **Jun571** against enteroviruses[31], we aimed to further advance this series of compounds to the EV-D68 infection mouse model studies. For this, we conducted a structure-property relationship optimization to improve their mouse liver microsomal stability. The initial lead compound **Jun571** had moderate microsomal stability with a $T_{1/2}$ of 21.3 min. Computational metabolite prediction suggested that the amide bond and the tertiary amine are susceptible to hydrolysis and demethylation, respectively[34]. Therefore, we focused on increasing the steric hindrance on the ethyl linker to mitigate metabolism. All designed inhibitors contain a terminal positive charged amine to maintain the ionic hydrogen bonding interactions with Asp160 or Asp183, a critical feature for the high affinity binding to EV-D68 2C as inferred by the MD simulations (Fig. 1). Consistent with our hypothesis, compounds with sterically hindered linkers such as **Jun51062**, **Jun51064**, **Jun6504**, **Jun1073**, **Jun6962**, **Jun9352**, **Jun6952**, and **Jun9351** had improved microsomal stability with the $T_{1/2}$ from 70.1 to >145 min (Fig. 2a). Compounds with a primary amine were generally more metabolically stable than compounds with secondary and tertiary amines (**Jun5532** vs **Jun5251**, **Jun5553**, and **Jun5523**; **Jun5253** vs **Jun571** and **Jun5174**; **Jun9352** vs **Jun8944**). Nevertheless, azetidine-containing inhibitors with secondary amines are also highly metabolically stable (**Jun51062**, **Jun51064**, **Jun6504**, and **Jun1073**) (Fig. 2a).

The 2C protein is a conserved viral protein among enteroviruses (Supplementary Fig. 1), and it is expected that 2C inhibitors will display broad-spectrum antiviral activities. To validate this hypothesis, we tested **Jun51064**, **Jun6504**, **Jun6962**, **Jun9351**, **Jun9352**, and **Jun10241** against EV-A71 Tainan and CVB3 Nacy strains in plaque assays. It was found that these 2C inhibitors retained potent antiviral activities against EV-A71 ($EC_{50} = 0.27$ to $0.61\,\mu M$) and CVB3 ($EC_{50} = 0.18$ to $2.03\,\mu M$) (Fig. 2b, c).

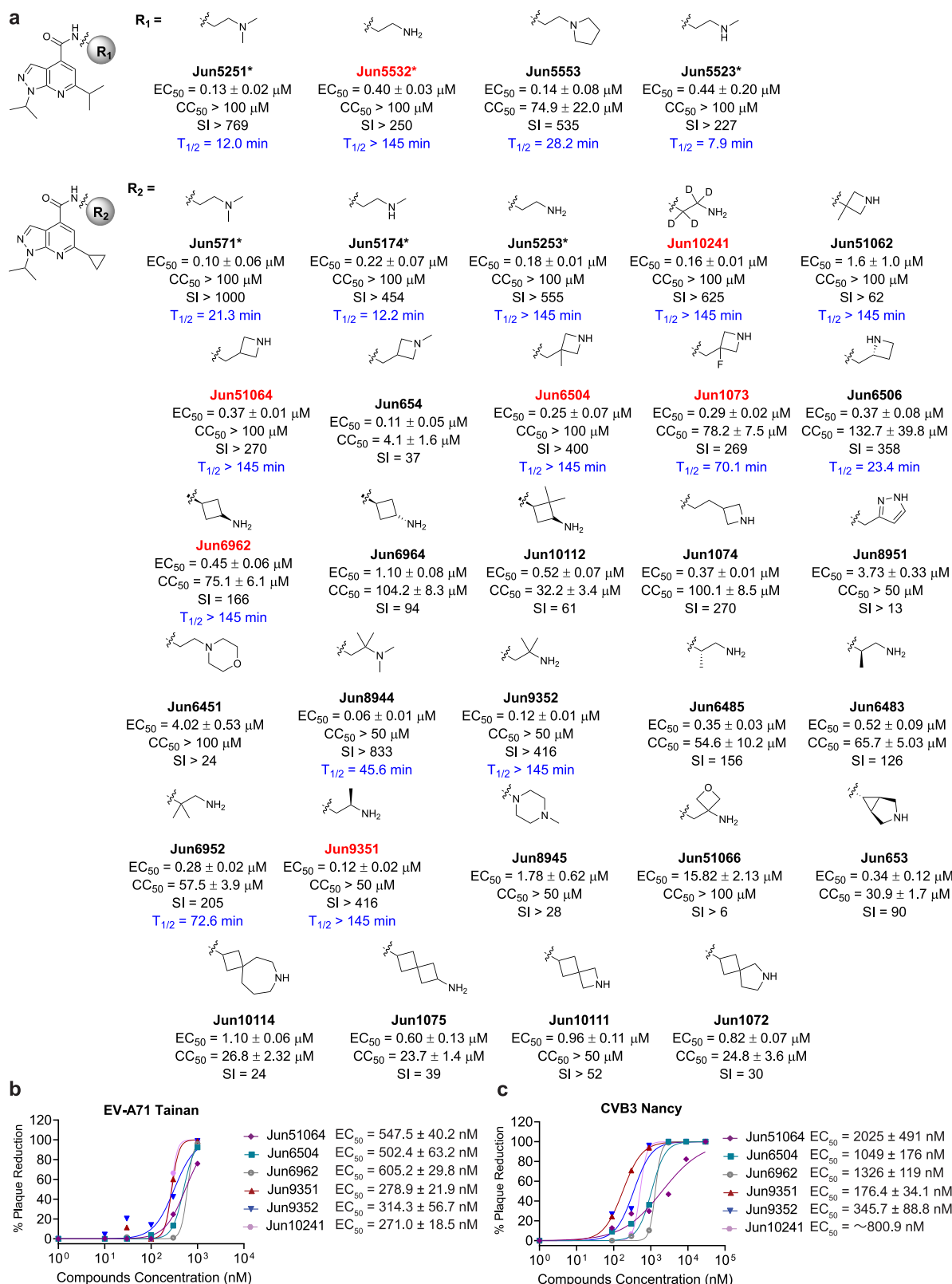## In vivo pharmacokinetic (PK) properties of 2C inhibitors in mice

To select lead candidates for the in vivo antiviral efficacy study, we profiled the in vivo PK properties of 2C inhibitors showing potent antiviral activity and high microsomal stability, including **Jun5532**, **Jun10241**, **Jun6504**, **Jun9351**, and **Jun6962**. The original lead compound **Jun571** was included as a control. Each compound was administered to female BALB/c mice ($n = 5$) at 30 or 50 mg/kg by intraperitoneal (i.p.) injection. The plasma concentration of compounds at each time point was determined by LC–MS/MS using multiple reaction monitoring (MRM) at m/z 290.2/231.1 (**Jun5532**), 292.0/275.2 (**Jun10241**), 328.1/299.1 (**Jun6504**), 302.1/243.1 (**Jun9351**), and 314.2/228.2 (**Jun6962**), respectively. For the quantification of each compound, a calibration curve was constructed using the pure compound via linear regression. The correlation coefficient values of all the compounds in plasma were >0.99 for a range of 20-4000 ng/mL. The limit of quantification (LOQ) was 20 ng/mL with the signal to noise >10:1. The recovery of all compounds was more than 80% under the current sample preparation method. The pharmacokinetic profiles of **Jun6504** series of compounds are shown in Fig. 3a, b, and their pharmacokinetic parameters are shown in Fig. 3c.

Jun6504 series of compounds were quickly absorbed in vivo and reached the maximum plasma concentration at around 1 h (T_{max}) after i.p. injection. The clearance of **Jun6504** series compounds was also relatively fast, with half-lives ($t_{1/2}$) of around 2–3 h. After i.p. injection at 50 mg/kg, the peak plasma concentration (C_{max}) of **Jun5532**, **Jun10241**, and **Jun6504** were 2838, 2642, and 2302 ng/mL, respectively. And the area under the concentration-time curve (AUC) of **Jun5532**, **Jun10241**, and **Jun6504** were 7605, 10730, and 11124 ng/mL*h, respectively. After i.p. injection at 30 mg/kg, the C_{max} of **Jun9351** and **Jun6962** were 2053 and 1432 ng/mL, respectively, and the AUC of **Jun9351** and **Jun6962** were 11,552 and 7398 ng/mL*h, respectively. In comparison, the original lead compound **Jun571** displayed relatively low plasma drug exposure with a C_{max} of 916 ng/ml following i.p. injection at 50 mg/kg (Supplementary Fig. 4). Based on the in vivo PK profiles, **Jun6504** was selected for mechanistic studies and the in vivo EV-D68 infection mouse model study.

Jun6504 displays broad-spectrum antiviral activity against enteroviruses

To profile the broad-spectrum antiviral activity of **Jun6504** against enteroviruses, **Jun6504** was tested against multiple enterovirus species, including five strains of EV-D68 isolated from the 2014 epidemic: clade B1 viruses US/MO/14-18947 and US/MO/14-18949, clade B2 viruses US/IL/14-18952 and US/IL/14-18956, and clade D virus US/KY/14-18953; enterovirus A species (EV-A71, CVA16, and CVA6); enterovirus B (CVB3); and enterovirus C (poliovirus type 1) in cell culture (Fig. 4a–c). **Jun6504** showed consistent antiviral activity against five strains of EV-D68 with EC_{50} values ranging from 0.25 to 0.47 μM (Fig. 4a). In addition, **Jun6504** exhibited dose-dependent inhibition against CVA16, CVA6, poliovirus type 1, and CVB3 in CPE assay with EC_{50} values from 0.24 to 0.57 μM (Fig. 4b). In the plaque assay, **Jun6504** dose-dependently inhibited EV-A71 and EV-D68 plaque formation in RD cells with EC_{50} values of 0.22 and 0.13 μM, respectively (Fig. 4c). **Jun6504** was not cytotoxic in Hela, RD, or Vero cells and had CC_{50} values greater than 100 μM (Fig. 4d).

To validate that the viral 2C protein is the drug target of **Jun6504**, we performed a differential scanning fluorimetry (DSF) assay to evaluate the direct binding of **Jun6504** to enterovirus 2C proteins. DSF is a widely used technique to assess protein stability, and ligand binding typically increases the stability of the target protein, resulting in a higher melting temperature (T_m)[35,36]. **Jun6504** displayed dose-dependent increases in melting temperatures of the EV-A71, EV-D68,

a

R₁ =

Jun5251*
EC₅₀ = 0.13 ± 0.02 μM
CC₅₀ > 100 μM
SI > 769
T₁/₂ = 12.0 min

Jun5532*
EC₅₀ = 0.40 ± 0.03 μM
CC₅₀ > 100 μM
SI > 250
T₁/₂ > 145 min

Jun5553
EC₅₀ = 0.14 ± 0.08 μM
CC₅₀ = 74.9 ± 22.0 μM
SI = 535
T₁/₂ = 28.2 min

Jun5523*
EC₅₀ = 0.44 ± 0.20 μM
CC₅₀ > 100 μM
SI > 227
T₁/₂ = 7.9 min

R₂ =

Jun571*
EC₅₀ = 0.10 ± 0.06 μM
CC₅₀ > 100 μM
SI > 1000
T₁/₂ = 21.3 min

Jun5174*
EC₅₀ = 0.22 ± 0.07 μM
CC₅₀ > 100 μM
SI > 454
T₁/₂ = 12.2 min

Jun5253*
EC₅₀ = 0.18 ± 0.01 μM
CC₅₀ > 100 μM
SI > 555
T₁/₂ > 145 min

Jun10241
EC₅₀ = 0.16 ± 0.01 μM
CC₅₀ > 100 μM
SI > 625
T₁/₂ > 145 min

Jun51062
EC₅₀ = 1.6 ± 1.0 μM
CC₅₀ > 100 μM
SI > 62
T₁/₂ > 145 min

Jun51064
EC₅₀ = 0.37 ± 0.01 μM
CC₅₀ > 100 μM
SI > 270
T₁/₂ > 145 min

Jun654
EC₅₀ = 0.11 ± 0.05 μM
CC₅₀ = 4.1 ± 1.6 μM
SI = 37

Jun6504
EC₅₀ = 0.25 ± 0.07 μM
CC₅₀ > 100 μM
SI > 400
T₁/₂ > 145 min

Jun1073
EC₅₀ = 0.29 ± 0.02 μM
CC₅₀ = 78.2 ± 7.5 μM
SI = 269
T₁/₂ = 70.1 min

Jun6506
EC₅₀ = 0.37 ± 0.08 μM
CC₅₀ = 132.7 ± 39.8 μM
SI = 358
T₁/₂ = 23.4 min

Jun6962
EC₅₀ = 0.45 ± 0.06 μM
CC₅₀ = 75.1 ± 6.1 μM
SI = 166
T₁/₂ > 145 min

Jun6964
EC₅₀ = 1.10 ± 0.08 μM
CC₅₀ = 104.2 ± 8.3 μM
SI = 94

Jun10112
EC₅₀ = 0.52 ± 0.07 μM
CC₅₀ = 32.2 ± 3.4 μM
SI = 61

Jun1074
EC₅₀ = 0.37 ± 0.01 μM
CC₅₀ = 100.1 ± 8.5 μM
SI = 270

Jun8951
EC₅₀ = 3.73 ± 0.33 μM
CC₅₀ > 50 μM
SI > 13

Jun6451
EC₅₀ = 4.02 ± 0.53 μM
CC₅₀ > 100 μM
SI > 24

Jun8944
EC₅₀ = 0.06 ± 0.01 μM
CC₅₀ > 50 μM
SI > 833
T₁/₂ = 45.6 min

Jun9352
EC₅₀ = 0.12 ± 0.01 μM
CC₅₀ > 50 μM
SI > 416
T₁/₂ > 145 min

Jun6485
EC₅₀ = 0.35 ± 0.03 μM
CC₅₀ = 54.6 ± 10.2 μM
SI = 156

Jun6483
EC₅₀ = 0.52 ± 0.09 μM
CC₅₀ = 65.7 ± 5.03 μM
SI = 126

Jun6952
EC₅₀ = 0.28 ± 0.02 μM
CC₅₀ = 57.5 ± 3.9 μM
SI = 205
T₁/₂ = 72.6 min

Jun9351
EC₅₀ = 0.12 ± 0.02 μM
CC₅₀ > 50 μM
SI > 416
T₁/₂ > 145 min

Jun8945
EC₅₀ = 1.78 ± 0.62 μM
CC₅₀ > 50 μM
SI > 28

Jun51066
EC₅₀ = 15.82 ± 2.13 μM
CC₅₀ > 100 μM
SI > 6

Jun653
EC₅₀ = 0.34 ± 0.12 μM
CC₅₀ = 30.9 ± 1.7 μM
SI = 90

Jun10114
EC₅₀ = 1.10 ± 0.06 μM
CC₅₀ = 26.8 ± 2.32 μM
SI = 24

Jun1075
EC₅₀ = 0.60 ± 0.13 μM
CC₅₀ = 23.7 ± 1.4 μM
SI = 39

Jun10111
EC₅₀ = 0.96 ± 0.11 μM
CC₅₀ > 50 μM
SI > 52

Jun1072
EC₅₀ = 0.82 ± 0.07 μM
CC₅₀ = 24.8 ± 3.6 μM
SI = 30

b

EV-A71 Tainan

Jun51064	EC₅₀ = 547.5 ± 40.2 nM
Jun6504	EC₅₀ = 502.4 ± 63.2 nM
Jun6962	EC₅₀ = 605.2 ± 29.8 nM
Jun9351	EC₅₀ = 278.9 ± 21.9 nM
Jun9352	EC₅₀ = 314.3 ± 56.7 nM
Jun10241	EC₅₀ = 271.0 ± 18.5 nM

c

CVB3 Nancy

Jun51064	EC₅₀ = 2025 ± 491 nM
Jun6504	EC₅₀ = 1049 ± 176 nM
Jun6962	EC₅₀ = 1326 ± 119 nM
Jun9351	EC₅₀ = 176.4 ± 34.1 nM
Jun9352	EC₅₀ = 345.7 ± 88.8 nM
Jun10241	EC₅₀ = ～800.9 nM

Fig. 2 | Structure-property relationship studies of the pyrazolopyridine series of EV-D68 2C inhibitors. a Antiviral EC₅₀ values were determined in the CPE assay with EV-D68 US/MO/14-18947 in RD cells. Cytotoxicity CC₅₀ values were determined using the neutral red uptake method in RD cells. The results are the mean ± standard deviation (SD) of two independent experiments with three repeats in each experiment. *The antiviral activity EC₅₀ values of **Jun5532** and **Jun5253** were reported earlier[31]. SI selectivity index. **b** Antiviral activity of selected 2C inhibitors against EV-A71 Tainan strain in plaque assay. **c** Antiviral activity of selected 2C inhibitors against CVB3 Nancy strain in plaque assay. The EC₅₀ values in the plaque assay are the mean ± SD of two biological replicates. Source data are provided as a Source Data file.
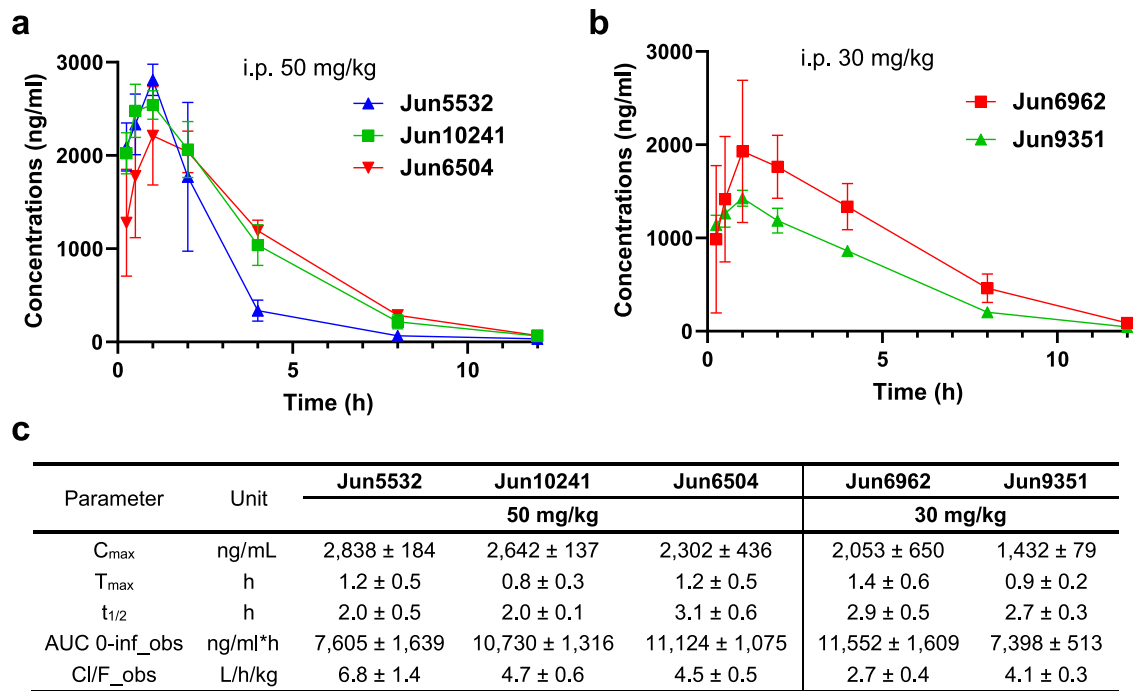
Fig. 3 | In vivo pharmacokinetic profiling of EV-D68 2C inhibitors in BALB/c mice. a In vivo clearance of **Jun5532**, **Jun10241**, and **Jun6504** in female BALB/c mice ($n = 5$) after i.p. injection at 50 mg/kg. Error bars denote mean ± SD of five biological replicates. **b** In vivo clearance of **Jun6962** and **Jun9351** in female BALB/c mice ($n = 5$) after i.p. injection at 30 mg/kg. Error bars denote mean ± SD of five biological replicates. **c** Pharmacokinetic parameters. The values represent mean ±

SD of five biological replicates. Adult female BALB/c mice were given a single i.p. injection at either 50 or 30 mg/kg. Blood samples were collected up to 12 h after administration of the compound. The plasma concentrations of inhibitors and the internal standard were analyzed by LC–MS/MS. Source data are provided as a Source Data file.

Parameter	Unit	Jun5532	Jun10241	Jun6504	Jun6962	Jun9351
		50 mg/kg			30 mg/kg	
C_{max}	ng/mL	2,838 ± 184	2,642 ± 137	2,302 ± 436	2,053 ± 650	1,432 ± 79
T_{max}	h	1.2 ± 0.5	0.8 ± 0.3	1.2 ± 0.5	1.4 ± 0.6	0.9 ± 0.2
$t_{1/2}$	h	2.0 ± 0.5	2.0 ± 0.1	3.1 ± 0.6	2.9 ± 0.5	2.7 ± 0.3
AUC 0-inf_obs	ng/ml*h	7,605 ± 1,639	10,730 ± 1,316	11,124 ± 1,075	11,552 ± 1,609	7,398 ± 513
Cl/F_obs	L/h/kg	6.8 ± 1.4	4.7 ± 0.6	4.5 ± 0.5	2.7 ± 0.4	4.1 ± 0.3

and CVB3 2C proteins (Fig. 4e). Next, a drug time-of-addition experiment was employed to elucidate which step(s) in the viral life cycle is affected by **Jun6504**. The EV-D68 US/MO/14-18947 virus was amplified in RD cells, and 3 μM of **Jun6504** was added at various time points during a single viral replication cycle (Fig. 4f)[37]. The period **Jun6504** was present in cell culture in the time-of-addition experiment was listed in parenthesis: −1 h (−1 to 14 h), −1' hr (−1 to 0 h), 0 h (0 to 14 h), 1 h (1 to 14 h), 3 h (3 to 14 h), 5 h (5 to 14 h), and 7 h (7 to 14 h). It was found that **Jun6504** completely inhibited EV-D68 amplification when added before or at 3 h post-infection (hpi) (Fig. 4g). A significant reduction in the antiviral potency of **Jun6504** was observed when added at 5 hpi, with almost complete loss of efficacy occurring at 7 hpi. These findings suggest that **Jun6504** blocks viral replication at an intermediate stage in the viral life cycle, corroborating the role of 2C in mediating viral RNA replication.

Serial viral passage experiment identified mutations in the 2C protein conferring drug resistance against Jun6504

To independently investigate the mechanism of action of **Jun6504**, we performed a serial passage experiment to select drug-resistant mutations against **Jun6504**. In the passage experiment, EV-D68 US/MO/14-18947 virus was amplified in RD cells with increasing concentrations of **Jun6504**, starting from approximately 1 × EC$_{50}$ of **Jun6504** at passage 1 (P1), followed by a twofold increase in each subsequent passage (Fig. 5a). The EC$_{50}$s of **Jun6504** against P3, P6, and P9 viruses were determined in CPE assay as 0.80, 3.38, and 15.45 μM, respectively (Fig. 5a). These values correspond to a 6.2-, 26-, and 118.8-fold increase, respectively, compared to P0 virus, indicating varying degrees of resistance might have evolved. Whole viral genome sequencing identified mutations within the viral 2C protein, specifically D323G at P3, D183V/ D323G/I112V (partial) at P6, and D183V/ D323G/I112V at P9 (Fig. 5b). These findings indicate that the viral 2C protein might be the primary target for **Jun6504**. To further validate this resistance

phenotype, recombinant EV-D68 viruses containing these 2C mutations were generated using a previously established reverse genetics system[38]. The drug sensitivity of **Jun6504** was assessed against these recombinant viruses in a plaque assay (Fig. 5c). Among the mutants tested, r2C-I112V/D183V/D323G exhibited the highest level of resistance to **Jun6504**, with an EC$_{50}$ of 3.77 μM, a 29-fold increase compared to the wild-type virus (rWT). Both r2C-D183V and r2C-D183V/ D323G mutants displayed high levels of resistance, with EC$_{50}$ values of 1.27 and 2.58 μM, respectively, corresponding to 9.8- and 19.8-fold increases compared to rWT virus. In contrast, r2C-I112V and r2C-D323G mutants exhibited only moderate resistance to **Jun6504**, with EC$_{50}$ values of 0.22 μM and 0.46 μM, respectively, representing 1.7- and 3.5-fold increases compared to rWT virus. These findings suggest that the 2C-D183V mutation is the predominant contributor to drug resistance, while mutations I112V and D323G confer resistance to a lesser extent, and the combination of these three mutants further increases the drug resistance level.

We further characterized the binding of **Jun6504** to EV-D68 2C and its mutants in the thermal shift assay. When tested at 30 μM, **Jun6504** displayed minimal stabilization of 2C-D183V ($\Delta T_m = 0.39$ °C) or 2C-D183V/D323G ($\Delta T_m = 0.12$ °C) mutants (Fig. 5d). Conversely, the binding of **Jun6504** to the 2C-D323G mutant was comparable to the WT, exhibiting a ΔT_m of 2.4 °C. The thermal shift assay results (Fig. 5d) corroborate the antiviral assay (Fig. 5c), showing that the D183V is the major drug-resistant mutant.

To elucidate the mechanism of drug resistance, we performed molecular docking calculations and 500 ns-MD simulations of **Jun6504** binding to EV-D68 2C and the D183V mutant (Fig. 5e–j). For the simulations, we generated the **Jun6504**-EV-D68 2C complex model based on the X-ray structure of (S)-fluoxetine−CVB3 2C complex structure (PDB ID 6S3A)[16] instead of the apo structure predicted by the Alphafold 3 (Supplementary Fig. 5). The superimposed X-ray crystal structures of EV-A71 2C/ATPγS (purple, apo) (PDB: 5GRB) and (S)-
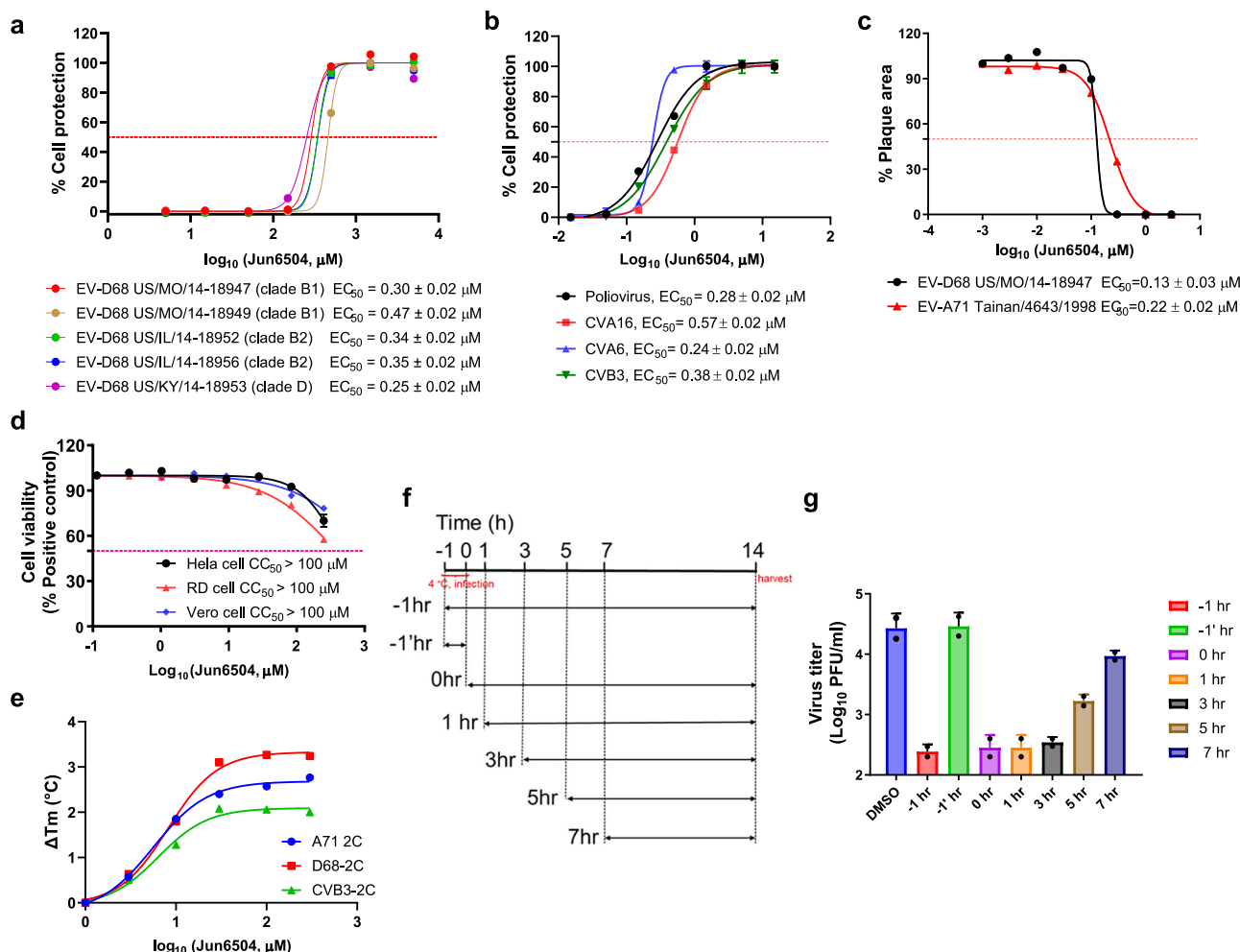
Fig. 4 | Broad-spectrum antiviral activity of Jun6504 against enteroviruses.
a Antiviral activity of **Jun6504** against five contemporary EV-D68 strains in RD cells. EC_{50} values against EV-D68 strains were determined using the cytopathic effect (CPE) assay in RD cells after 60 h of compound incubation. The EC_{50} values are the mean ± SD of three biological replicates. **b** Antiviral activity of **Jun6504** against poliovirus, CVA16, CVA6, and CVB3 in CPE assay. The EC_{50} values are the mean ± SD of two biological replicates. **c** Antiviral activity of **Jun6504** against EV-A71 and EV-D68 in plaque assay. The EC_{50} values are the mean ± SD of two biological replicates.

d Cytotoxicity of **Jun6504** in HeLa, RD, and Vero cells. The results are from two biological replicates. **e** DSF assay of **Jun6504** with EV-A71, EV-D68, and CVB3 2 C proteins. The results are from two biological replicates. **f Jun6504** time-of-addition experiment in a single cycle of EV-D68 replication. **g** Viral titers in the time-of-addition experiment. EC_{50} and CC_{50} curve fittings using $\log_{10}$ (concentration of **Jun6504**) vs. percentage of positive control with variable slopes were performed in Prism 8. Error bars denote mean ± SD of two biological replicates. Source data are provided as a Source Data file.

fluoxetine−CVB3 2C complex (gray, bound) (PDB: 6S3A) showed that drug binding induced a significant conformational change in the α2 helix (tilted by ~20.2° as indicated by the red arrow) (Supplementary Fig. 5a). As such, it was more logical to use the homology model of **Jun6504**-EV-D68 2C complex instead of the apo structure from Alphafold 3 for the MD simulations. The superimposed structures of Alphafold 3-generated apo EV-D68 2C protein (green, apo) and the homology model of **Jun6504**-EV-D68 2C (blue, bound) similarly showed a drug binding induced conformational change in the α2 helix (Supplementary Fig. 5b).

The starting pose of **Jun6504** in EV-D68 2C was generated by Schrödinger Glide extra precision (XP) docking. The top five poses were superimposable with variations only at the terminal dimethyllammonium (Supplementary Fig. 5c).

The starting and final binding poses in MD simulations match well showing that the ligand did not deviate significantly after the MD simulations from the starting docking pose (Supplementary Fig. 6). The MD simulations showed that the terminal secondary protonated amine group from **Jun6504** forms hydrogen bonding with Asp183 and Asp186 side chain carboxylate groups (Fig. 5e, f). Compared to **Jun571**,

the hydrogen bonding interactions with the Asp160 side chain carboxylate group are significantly suppressed, while the ionic character of the hydrogen bond with Asp183 is significantly diminished due to the steric hindrance from the azetidine group. The amide carbonyl forms a hydrogen bond with Met179 main chain amide NH, and the amide NH from **Jun6504** forms a water-mediated hydrogen bond with Asp186 side chain carbonyl. Similarly, with **Jun571**, the *N*-isopropyl from **Jun6504** fits in a hydrophobic pocket consisting of side chains from Ile126, Phe190, Ile127, Leu238, and Phe242, forming significant hydrophobic interaction mainly with Phe190 (Fig. 5e, f). The 6-cyclopropyl of the pyrazole forms hydrophobic interactions with Met189, while the pyrazole ring is surrounded by hydrophobic amino acid side chains, e.g., Met175, Leu178, Pro182, and Tyr163. The D183V mutation abolishes the electrostatic interaction between the Asp183 side chain carboxylate and the terminal amine from **Jun6504**, conferring drug resistance (Fig. 5h–j).

We also performed perturbative relative binding free energy calculations to quantify the effect of the D183V mutation on the binding of **Jun571** or **Jun6504** to EV-D68 2C; the results of the free energy calculations revealed relative binding free energy $\Delta\Delta G_{b,TI/MD}$ Jun571
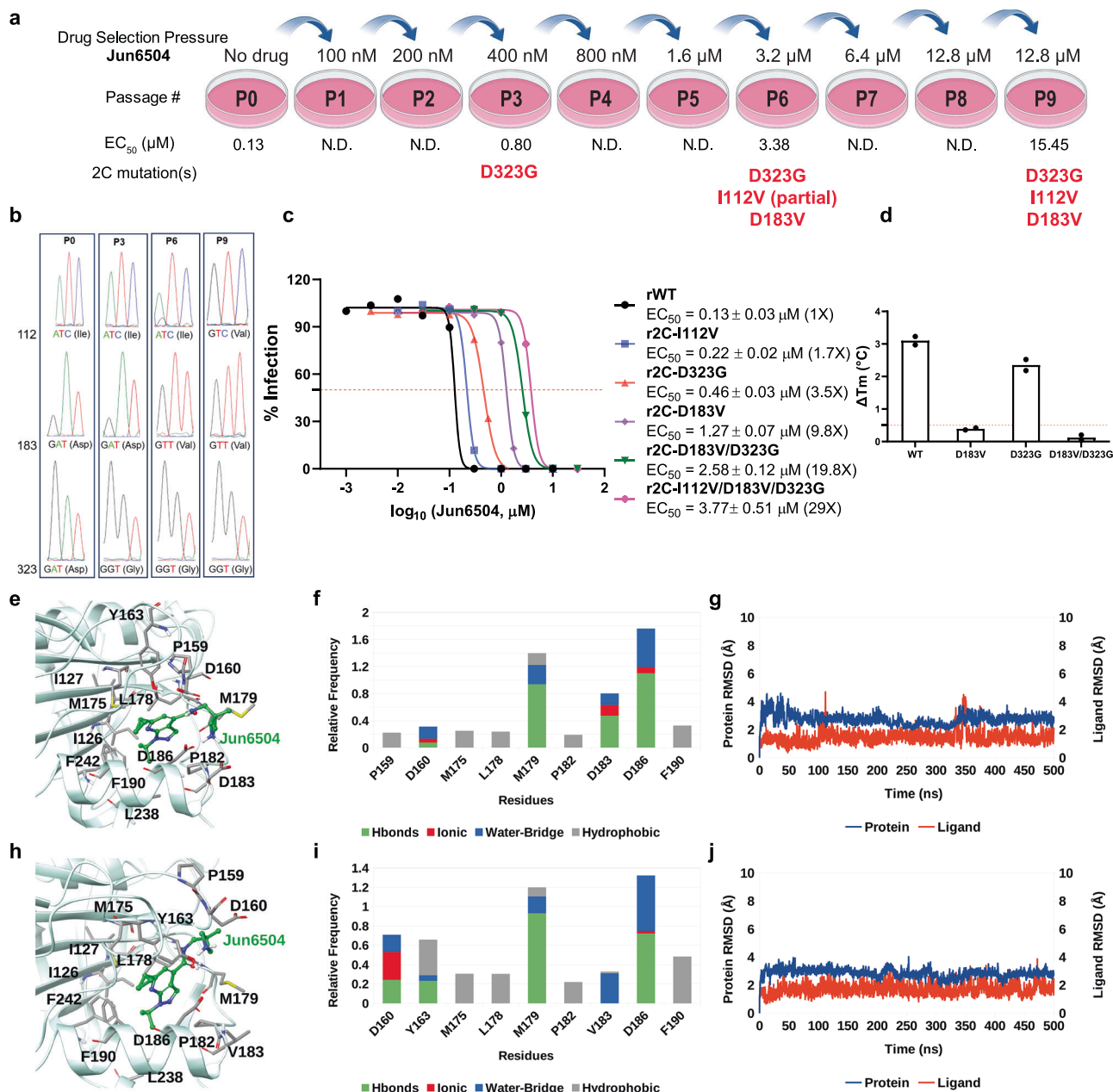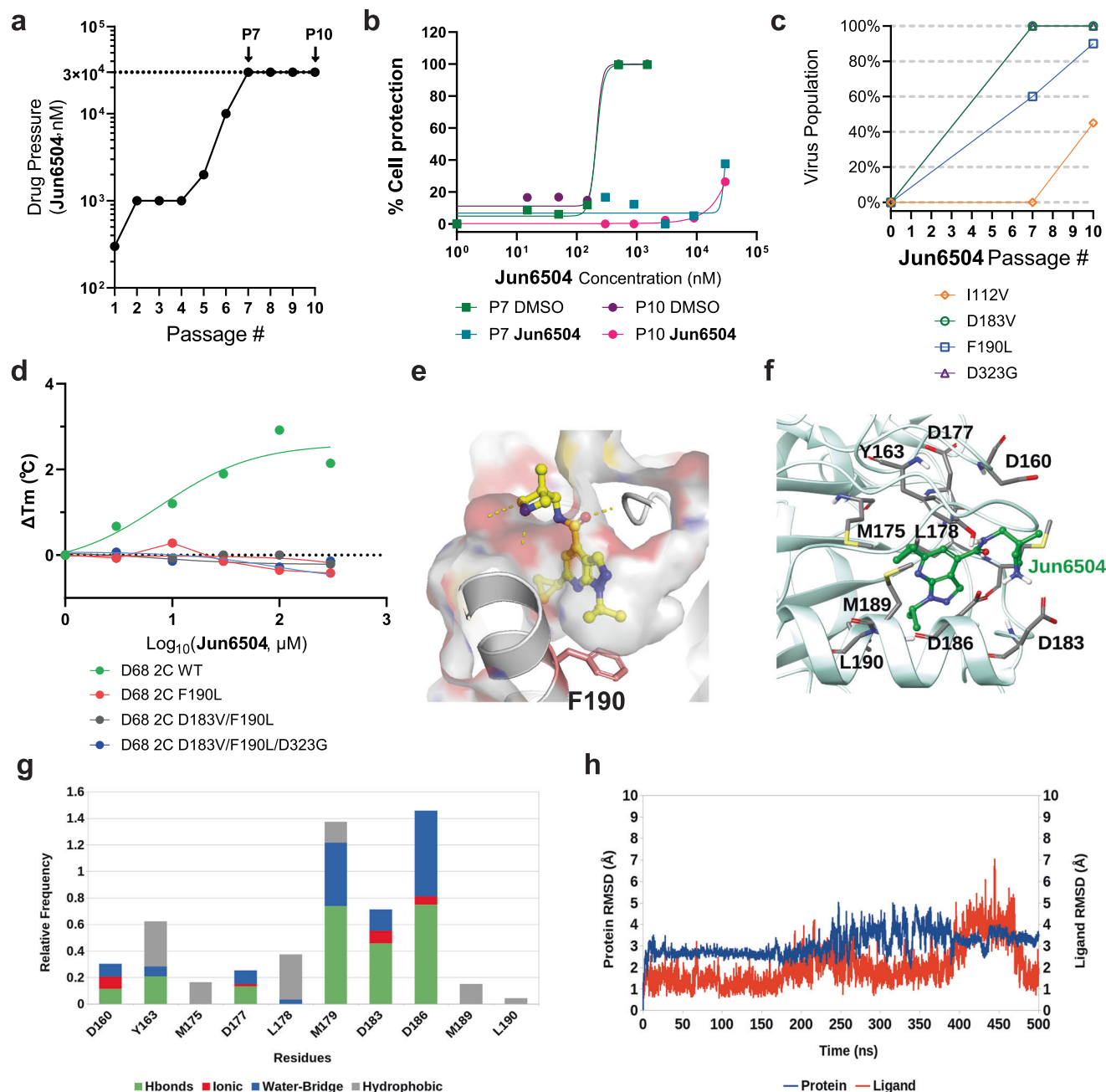
Fig. 5 | Serial viral passage experiments to identify drug-resistant mutants against EV-D68 2C inhibitor Jun6504 and MD simulations of Jun6504 with EV-D68 2C WT and D183V mutant. a Schematic illustration of the serial passage of **Jun6504** in RD cells with EV-D68 US/MO/14-18947. The graph was created with Biorender.com. Li, K (2025) https://BioRender.com/0kxixma. **b** Electropherogram traces of 2C protein coding region at residues 112, 183, and 323 from viruses at passages 0, 3, 6, and 9. **c** Antiviral EC_{50} curves of **Jun6504** against recombinant EV-D68 viruses in plaque assay. The EC_{50} values are mean ± SD from two biological replicates. **d** Thermal shift binding assay of **Jun6504** with EV-D68 2C WT, D183V, D323G, and D183V/D323G. The red line indicates a 0.5 °C shift ($\Delta Tm = 0.5$ °C). A ΔTm greater than 0.5 °C generally indicates ligand binding to the protein[69]. The assay was performed in two biological replicates. **e** Interactions between **Jun6504**

and the residues at the allosteric site of EV-D68 2C. **f** Stabilizing interactions inside the binding area of 2C with **Jun6504**; hydrogen bonding interactions bar is depicted in green, ion hydrogen bonding interactions in red, water bridges in blue, and lipophilic interactions in gray. **g** RMSD plots of Cα carbons of 2C (blue diagram) and of the heavy atoms of the ligand **Jun6504** (red diagram). **h** Interactions between **Jun6504** and the residues at the allosteric site of EV-D68 2C-D183V. **i** Stabilizing interactions inside the binding area of 2C-D183V with **Jun6504**; hydrogen bonding interactions bar is depicted in green, ion hydrogen bonding interactions in red, water bridges in blue and lipophilic interactions in gray. **j** RMSD plots of Cα carbons of 2C-D183V (blue diagram) and of the heavy atoms of the ligand **Jun6504** (red diagram). Source data are provided as a Source Data file.

(D183V) = 0.99 ± 0.17 kcal/mol and $\Delta\Delta G_{b,TI/MD\ Jun6504}$ = 1.60 ± 0.19 kcal/mol for **Jun571** and **Jun6504**, respectively, in agreement with experimental results.

As EV-D68 2C-D183V only leads to partial drug resistance against **Jun6504** (Fig. 5c), we were interested to see whether additional mutation(s) can lead to complete resistance. For this, we performed another independent round of serial viral passage experiment with

escalating drug selection pressure of **Jun6504** (Fig. 6a). Complete drug resistance was observed at P7 and P10 of **Jun6504**-treated viruses with antiviral EC_{50} values greater than 30 μM (Fig. 6b), while the DMSO-treated viruses at P7 and P10 remained sensitive to **Jun6504**. Sequencing the viral genome of the drug-resistant P7 and P10 viruses revealed several 2C mutations, including I112V, D183V, F190L, and D323G. While the I112V, D183V, and D323G mutations were consistent

Fig. 6 | Additional serial viral passage experiment to identify drug-resistant mutants against EV-D68 2C inhibitor Jun6504. a Schematic illustration of the serial passage of **Jun6504** in RD cells with EV-D68 US/MO/14-18947. **b** Antiviral EC_{50} curves of **Jun6504** against **Jun6504**-treated and DMSO-treated viruses at P7 and P10. The assay was performed in two biological replicates. **c** Sequencing results of the 2C protein from **Jun6504**-treated viruses at P7 and P10. **d** DSF binding assay of **Jun6504** against EV-D68 2C WT, F190L. D183V/F190L, and D183V/F190L/D323G. The assay was performed in two biological replicates. **e** Docking model of **Jun6504** in EV-D68 2C. **f** Interactions between **Jun6504** and the residues at the allosteric site of EV-D68 2C-F190L mutant. **g** Stabilizing interactions inside the binding area of EV-D68 2C-F190L with **Jun6504**; hydrogen bonding interactions bar is depicted in green, ion hydrogen bonding interactions in red, water bridges in blue and lipophilic interactions in gray. **h** RMSD plots of Cα carbons of EV-D68 2C-F190L (blue diagram) and of the heavy atoms of the ligand **Jun6504** (red diagram). Source data are provided as a Source Data file.

with the previous passage experiment (Fig. 5a), the F190L mutation was a new finding. The DSF binding assay showed that the F190L-containing single (F190L), double (D183V/F190L), and triple (D183V/F190L/D323G) EV-D68 2C mutant proteins were completely resistant to **Jun6504** (Fig. 6d), indicating that F190L is responsible for complete drug resistance. F190 is located at the α2 helix and forms hydrophobic interactions with the isopropyl substituent in **Jun6504** (Fig. 6e), and F190L likely causes a steric clash with the inhibitor, leading to drug resistance. To validate this hypothesis, we performed 500-ns-MD

simulations of **Jun6504** with the EV-D68 2C-F190L mutant. The results showed that the F190L mutation causes a destabilization of the ligand due to the loss of hydrophobic interactions between the P190 phenyl with the N-isopropyl from **Jun6504** (Fig. 6f–h). We further performed perturbative relative binding free energy calculations, and the results of the free energy calculations revealed a significant positive value $\Delta\Delta G_{b,TI/MD}$ $_{Jun6504}$(P190L) = 3.81 ± 0.09 kcal/mol, compared to the $\Delta\Delta G_{b,TI/MD}$ $_{Jun6504}$(D183V) = 1.60 ± 0.19 kcal/mol. Collectively, the relative binding free energies agree with the antiviral and DSF binding

assay results, showing that P190L is more resistant than D183V against **Jun6504**.

It is worth noting that the F190L mutation was also reported to confer (S)-fluoxetine resistance against CVB3 2C[16,17]. These results further demonstrated that **Jun6504** targets the same allosteric binding pocket in 2C as (S)-fluoxetine.

We also attempted to generate the recombinant EV-D68 viruses with either the F190L single mutation (r2C-F190L) or the I112V/D183V/F190L/D323G quadruple mutations (r2C-I112V/D183V/F190L/D323G). However, we failed to recover the viruses. We are unsure about the exact reason since we were able to rescue the WT recombinant viruses each time. Instead, we performed plaque purification of the P10 virus mixture from the passage experiment and selected 12 colonies of viruses (Supplementary Fig. 7). We sequenced their 2C genes and selected two colonies: clone 9 with the 2C-M179L/D183V/F190L/D323G mutant and clone 10 with the 2C-I112V/D183V/F190L/D323G mutant. The recombinant EV-D68 virus with the 2C-I112V/D183V/D326G had an EC_{50} of 3.77 μM against **Jun6504**, a 29-fold increase from the WT (Fig. 5c). The plaque purified EV-D68 virus (clone 10) with the 2C-I112V/D183V/F190L/D323G mutant had an EC_{50} value the over 50 μM, suggesting that F190L further increased the drug resistance.

Jun6504 is effective at protecting mice from EV-D68 infection-induced paralysis

Neonatal mice were infected with EV-D68 by intramuscular injection into the left quadriceps muscle. Using this previously published neonatal mouse model[21], the US/IL/14-18952 isolate of EV-D68 reliably produces paralysis beginning 4–6 days post-infection in the left hindlimb, followed by paralysis in the right hindlimb and sometimes paralysis of the forelimbs[39]. In this model, paralysis scores stabilize by 11 days post-infection, and the scores remain stable for at least 28 days following infection. Animals that were treated with **Jun6504** (via i.p. injection at 50 mg/kg) immediately following intramuscular infection, with injections continuing daily for 14 days, had significantly lower paralysis scores and significantly increased body weight gain compared to animals injected with "no drug" control (Fig. 7a, b). When treatment was initiated at 24 h post-infection and continued daily for 13 days (24-h delayed model), animals treated with **Jun6504** again had significantly lower paralysis scores and significantly increased body weight gain compared to animals injected with "no drug" control (Fig. 7c, d). The mice tolerated the 50 mg/kg dose well, and no signs of pain, weight loss, or death were observed in uninfected **Jun6504-treated** animals.

To examine how **Jun6504** affects viral titer in the muscle and spinal cord, we collected quadriceps muscles and spinal cords from EV-D68-infected pups at 1- and 5-days post-infection (DPI). A pictographic representation of the dosing regimen, tissue collection time points, and age of pups is shown in Fig. 7e. For these tissue collections, mice were treated according to the 24-h delayed treatment model. Approximately 10^4 $TCID_{50}$ (50% tissue culture infectious dose) was present in untreated mice's left quadriceps muscle at 24 h post-infection (Fig. 7f). However, by 5 days post-infection (after 4 daily doses of **Jun6504**), the left quadriceps muscle of "no drug" control animals had significantly higher viral titers than the left quadriceps muscle of **Jun6504**-treated animals (~10^5 $TCID_{50}$ vs 10^4 $TCID_{50}$ respectively) (Fig. 7f). The right quadriceps muscle, contralateral to the virus injected quadriceps muscle, did not have measurable viral titer at either 1- or 5-days post-infection (data not shown). No detectable virus was present in the spinal cord of untreated animals at 24-h post-infection (DPI1, prior to **Jun6504** treatment). At 5 days post-infection (DPI5, after 4 daily doses of **Jun6504**), there was significantly less virus in the spinal cords of **Jun6504**-treated animals compared to the "no drug" treated control animals (Fig. 7g). To examine whether **Jun6504** was able to cross the blood–brain barrier, we examined the concentration of the drug in the spinal cords of treated and untreated

animals. One hour after the intraperitoneal injection of **Jun6504**, mice had approximately 575 ng drug/g of tissue in the spinal cord, whereas no detectable drug was found in the spinal cords of untreated animals (Fig. 7h).

To examine whether the improved paralysis scores in the **Jun6504-treated** animals were due to improved motor neuron survival in this group, we performed immunohistochemistry (IHC) staining of the lumbar spinal cord sections from treated and untreated animals. All IHC stains were done at 8 DPI in animals treated using the 24-h delayed treatment model. We found that in the "no drug" control group, animals with a paralysis score of 6 (complete paralysis in both hindlimbs) had no choline acetyltransferase (ChAT) positive motor neurons evident in the lumbar spinal cord region (Fig. 8b). In contrast, when the same region was examined in **Jun6504**-treated animals, with a paralysis score of 0, there were many ChAT-positive motor neurons present (Fig. 8a). We also noted an apparent loss of neuronal nuclei (NeuN) positive neurons in "no drug" controls that were not present in the **Jun6504**-treated animals (green stain in Fig. 8a vs b). As noted previously, in this neonatal mouse model for EV-D68, the hindlimbs develop paralysis a few days prior to the forelimbs. To examine whether the virus had reached the cervical spinal cord in the "no drug" control group, we conducted IHC staining for EV-D68 VP2 and found that EV-D68-infected (NeuN+) neurons were present in the cervical enlargement of "no drug" controls (Fig. 8c). In contrast, no infected (NeuN+) neurons were observed in the cervical enlargement of **Jun6504**-treated animals (data not shown). Given the loss of NeuN+ neurons and ChAT+ motor neurons from the lumbar enlargement of "no drug" control animals, and the presence of EV-D68-infected cells in the cervical enlargement of these animals, it suggests that viral infection has destroyed the permissive cells from the lumbar region of untreated animals and active infection has successfully moved on to the cervical region. Alternatively, given the presence of NeuN+ nuclei and ChAT+ motor neurons in the lumbar region of **Jun6504**-treated animals and the lack of EV-D68 VP2 in the cervical enlargement, it suggests that infection has not moved on to the cervical region in **Jun6504**-treated animals. Consistent with this, we did observe EV-D68 VP2-positive neurons in the lumbar enlargement of **Jun6504**-treated animals (Fig. 8d), suggesting active infection was still limited to the lumbar region of **Jun6504**-treated animals.

Discussion

EV-D68-induced paralysis is a rare but severe disease. With the increased neurovirulence of contemporary EV-D68 strains, there is a dire need to develop vaccines and antiviral drugs. Drug repurposing identified multiple promising drug candidates against EV-D68 in cell culture, but unfortunately, very few displayed in vivo antiviral efficacy in EV-D68-infected mouse models. In the present work, we employed a structure-based design and lead optimization to develop inhibitors targeting the viral 2C protein. We identified **Jun6504** as showing potent and broad-spectrum antiviral activity against enteroviruses, including EV-D68, EV-A71, CVB3, CVA6, CVA16, and poliovirus. Superposition of the X-ray crystal structure CVB3 2C onto the homology model of EV-D68 2C showed that they adopt a similar 3D structure (Supplementary Fig. 8), corroborating the broad-spectrum antiviral activity of Jun6504. **Jun6504** displayed favorable in vivo PK properties, rendering it suitable for the mouse model study. The thermal shift assay, MD simulations, and resistance selection collectively validated that **Jun6504** binds to the same allosteric site in viral 2C protein as (S)-fluoxetine[16]. **Jun6504** was well tolerated in mice and significantly improved paralysis score and weight gain, even when treatment was initiated 24 h post-infection. Examining drug concentration in the spinal cord indicates that **Jun6504** can penetrate the blood–brain barrier. Moreover, **Jun6504** treatment significantly reduces viral titer in the spinal cord at 5 DPI (when paralysis scores of untreated animals begin to increase quickly).
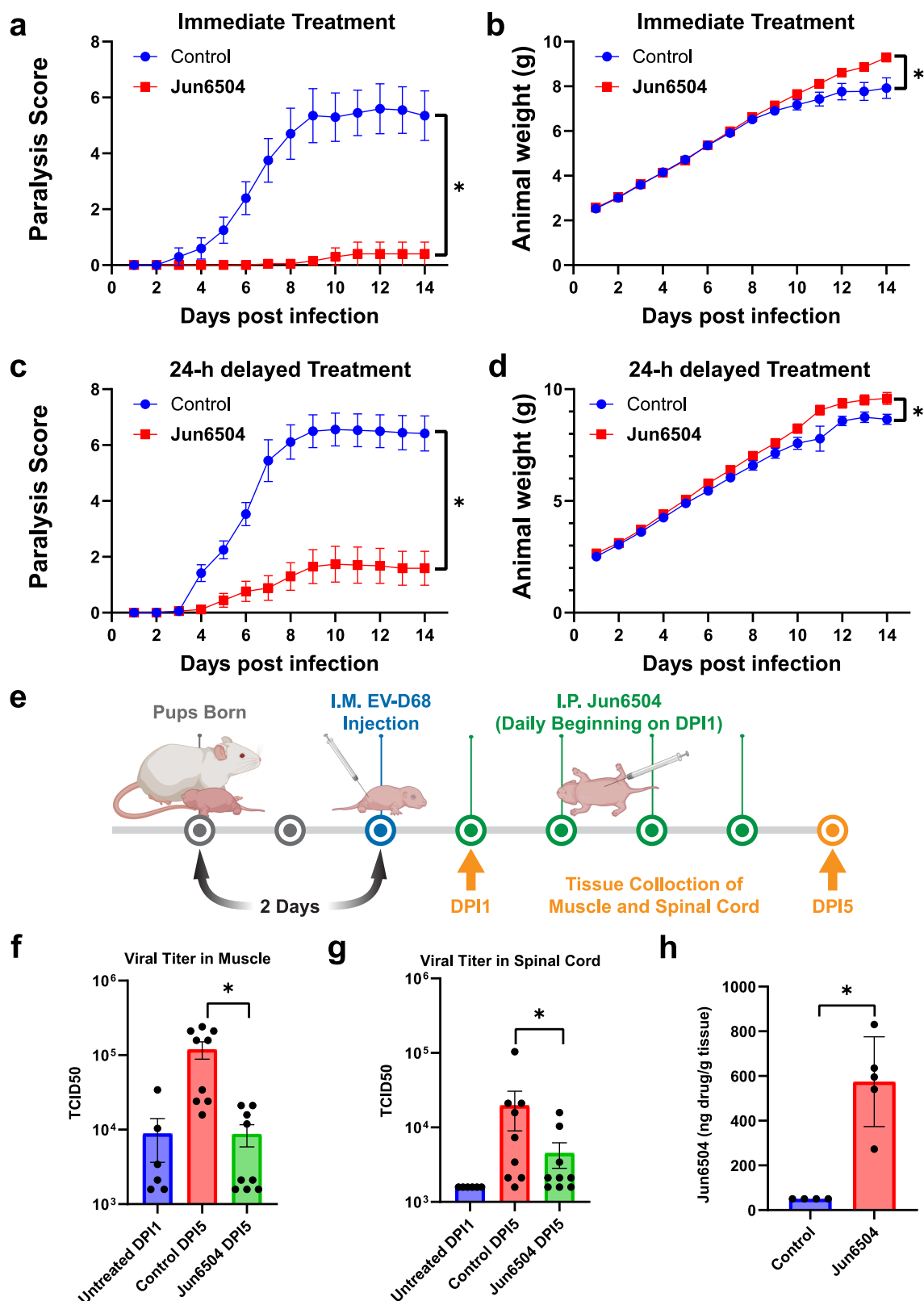
Jun6504 also significantly decreases viral titer in the infected quadriceps muscle at this same time point. The improvement in paralysis may be driven by the drug's efficacy in the muscle, spinal cord, or both. Examination of the lumbar enlargement (an enlarged region of the spinal cord containing motor neurons critical for hindlimb movement) showed complete loss of ChAT+ motor neurons in untreated animals with complete paralysis of the hindlimbs, whereas

the ChAT+ motor neurons were present in unparalyzed animals that had been treated with **Jun6504**. We also saw a marked loss of NeuN+ neurons from the lumbar enlargement of untreated animals. This data indicates that EV-D68 is destroying motor neurons and other neurons in the lumbar spinal cord. We observed EV-D68-infected cells in a wavefront immediately anterior to the "destroyed" spinal cord regions (characterized by a complete lack of NeuN and ChAT

Fig. 7 | Antiviral efficacy of Jun6504 in the EV-D68 infection mouse model. All control animals received vehicle alone (90% corn oil + 10% DMSO). All **Jun6504** groups received 50 mg/kg of **Jun6504** in the vehicle. All error bars represent SEM. **a** Paralysis scores are significantly lower in the **Jun6504** group in the immediate treatment model (*$p = 0.0004$ Wilcoxon rank-sum; Control $N = 10$ [DPI14 = 5.35 ± 0.89], **Jun6504** $N = 10$ [DPI14 = 0.40 ± 0.42]). **b** Weights from EV-D68-infected mice shown in Fig. a. Weight gain is also significantly increased by **Jun6504** (*$p = 0.003$ t-test, Control DPI14 = 7.92 ± 0.46 g vs **Jun6504** DPI14 = 9.29 ± 0.14 g). **c** Paralysis scores are significantly lower in **Jun6504** group in 24-h delayed treatment model (*$p = 0.0043$ Wilcoxon rank-sum; Control $N = 18$ [DPI14 = 6.42 ± 0.63], **Jun6504** $N = 17$ [DPI14 = 1.59 ± 0.61]). **d** Weights from the EV-D68-infected mice shown in Fig. c. Weight gain is also significantly increased by **Jun6504** (*$p = 0.0052$ t-test; Control DPI14 = 8.65 ± 0.23 g vs **Jun6504** DPI14 = 9.59 ± 0.27 g). **e** Pictorial representation of tissue harvest time points before treatment at DPI1 or after 4x daily injections on DPI5. The graph was created with Biorender.com. Li, K (2025) https://BioRender.com/kmwsykp.

f Viral titer in muscle tissue from left quadriceps (infected muscle) prior to treatment (blue bar) and after 4 days of treatment (red and green bars). There is significantly more virus in the quadriceps muscle from untreated pups at DPI5 compared to **Jun6504**-treated pups (pooled t-test *$p > 0.0001$; Control $N = 9$ mean $119{,}544 \pm 33{,}194 \, \mathrm{TCID}_{50}$ vs Jun6504 $N = 9$ mean $8762 \pm 3080 \, \mathrm{TCID}_{50}$). The limit of detection in this assay is $1580 \, \mathrm{TCID}_{50}$. **g** Viral titer in spinal cords from the same animals shown in panel (f). There is significantly more virus in the spinal cord of untreated pups at DPI5 compared to **Jun6504**- treated pups (pooled t-test *$p > 0.0484$; Control mean $19{,}834 \pm 11{,}519 \, \mathrm{TCID}_{50}$ vs **Jun6504** mean $4520 \pm 1796 \, \mathrm{TCID}_{50}$). All TCID_{50} values in untreated spinal cords from DPI1 are at the limit of detection. **h** Concentration of **Jun6504** in spinal cords collected from uninfected pups. **Jun6504** does enter the spinal cord (*$p = 0.0151$ Wilcoxon rank-sum, vehicle control $N = 4$ [50.0 ± 0.0] vs **Jun6504** $N = 5$ [574.6 ± 100.5]). All vehicle control data is at the limit of detection. All statistics shown in Fig. 7 are two-sided (**a–d**, **f–h**). Source data are provided as a Source Data file.
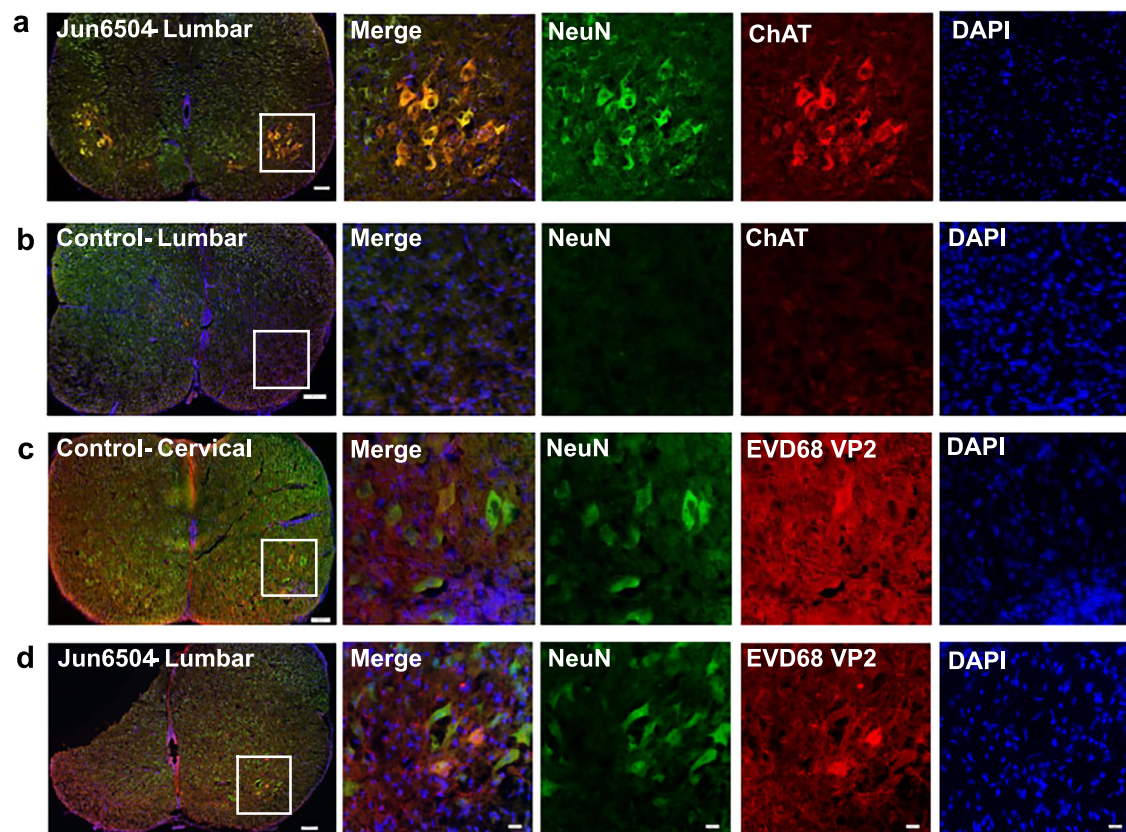
Fig. 8 | IHC stain of motor neurons in spinal cords from Jun6504-treated vs control (corn oil) treated mice collected at 8 days post-infection. a IHC stain of a transverse section through the lumbar spinal cord of **Jun6504**-treated animal with no paralysis in hindlimbs. Four panels to the right show increased zoom of the white dashed box where neuronal nuclei, choline acetyltransferase, and DAPI are green, red, and blue signals, respectively. **b** IHC stain of transverse section through lumbar spinal cord of corn oil control-treated animal with complete paralysis in both hindlimbs. Four panels to the right show increased zoom of the white dashed box where neuronal nuclei, choline acetyltransferase, and DAPI are green, red, and blue signals, respectively. **c** IHC stain of transverse section through cervical spinal cord of corn oil control-treated animal with complete paralysis in both hindlimbs, but no paralysis in forelimbs. Four panels to the right show an increased zoom of the white dashed box. Anti-neuronal nuclei is green, anti-Enterovirus D68 viral protein 2 is red, and DAPI is blue. **d** IHC stain of transverse section through lumbar spinal cord of **Jun6504**- treated animal with complete paralysis in left hindlimb, but no paralysis in the right hindlimb. Four panels to the right show an increased zoom of the white dashed box. Anti-neuronal nuclei is green, anti-Enterovirus D68 viral protein 2 is red, and DAPI is blue. Scale bars in all images are 100 microns in length. Five serial sections (separated by 200 μm intervals) were collected for each spinal cord. A single representative image is shown in Fig. 8, but $N = 5$ spinal cords were stained for ChAT and $N = 3$ were stained for VP2.

staining). Consistent with the sparing of motor neurons in the **Jun6504**-treated group, we observed infected cells in the cervical enlargement of untreated animals, but infected cells were only seen in the lumbar region of **Jun6504**-treated animals. This suggests that drug treatment markedly slows the anterior progression of infection and shows that **Jun6504** prevents the complete loss of motor neurons from the lumbar spinal cord and thus preserves motor function in the hindlimbs. Collectively, **Jun6504** represents a promising drug candidate for further development as an EV-D68 antiviral.

Methods
Molecular docking calculations
Ligands preparation. The structure of the **Jun571** and of the (S)-fluoxetine were generated by means of Maestro (Schrödinger Release

2020-4: Maestro, Schrödinger, LLC, New York, NY, 2020; Schrödinger Release 2020-4: LigPrep, Schrödinger, LLC, New York, NY, 2020), their protonation state was inspected using Epik (Schrödinger Release 2020-4: Epik, Schrödinger, LLC, New York, NY, 2020) at pH 7.4 and were subsequently minimized by means of Macromodel (Schrödinger Release 2020-4: MacroModel, Schrödinger, LLC, New York, NY, 2020) and the MMFF94 force field using the conjugate gradient (CG) method and a distance-dependent dielectric constant of 4.0 until a convergence value of $0.0001 \, kJ \, Å^{-1} \, mol^{-1}$ was reached.

Preparation of the protein—Jun571 complexes for the MD simulations. The X-ray structure of CVB3 2C protein in complex with (S)-fluoxetine (PDB ID 6S3A)[16] and the X-ray structure of the apo form of EV-A71 2C protein (PDB ID 5GQ1)[33] were used to build the protein models. The PDB ID 6S3A structure was superimposed with PDB ID 5GQ1, and then the protein with PDB ID 6S3A was deleted to prepare a complex between S-fluoxetine and EV-A71 2C protein. A homology model for EV-D68 2C protein in complex with (S)-fluoxetine was prepared using the structure with PDB ID 6S3A. All the protein complex structures were processed with the Protein Preparation Wizard in Schrödinger suite 2021 (Protein Preparation Wizard; Epik, Schrödinger, LLC, New York, NY, 2021) through which were performed, for example, missing hydrogen atoms addition, protein termini capping at N-end with acetyl and at C-end with N-methyl amide groups, optimal protonation states for histidine residues determination, restrained minimization that allows hydrogen atoms to be freely minimized, while allowing for sufficient heavy-atom movement to relax strained bonds, angles, and clashes. The most favored protonation states of ionizable residues at pH 7 in these complexes were assigned using Epik (Epik, Schrödinger, LLC, New York, NY, 2021).

The docking of Jun571 to CVB3 2C, EV-A71 2C, and EV-D68 2C proteins and of (S)-fluoxetine heavy atoms to the CVB3 2 C protein was carried out with Glide program 6 (Schrödinger Release 2020-4: Glide, Schrödinger, LLC, New York, NY, 2021) with the induced-fit method of Schrödinger suite 2021 (Induced-fit Docking, Schrödinger, LLC, New York, NY, 2021) and the standard protocol (standard precision) which allows flexibility of both the ligand and the entire binding site. The model of the X-ray structure of CVB3 2 C protein in complex with S-fluoxetine (PDB ID 6S3A) prepared as described was used as template structure. Thus, the grid boxes for the binding site were built considering the coordinates of S-fluoxetine. Docking of Jun571 against the three 2C proteins and of S-fluoxetine against the CVB3 2C protein was performed using a softened potential in which the van der Waals scaling factor was set at 0.5 for both receptor and ligand. The Prime refinement step was set on the side chain prediction of amino acid residues within 5 Å of the ligand. Subsequently, a minimization of the same set of residues and the ligand for each protein/ligand complex pose was performed. After this stage, any receptor structure in each pose reflects an induced fit to the ligand structure and conformation. For each ligand docked, a maximum of 20 poses was retained. The RMSD of the highest in score-docking pose of S-fluoxetine's heavy atoms to the CVB3 2C protein compared to the experimental binding pose in the X-ray structure with PDB ID 6S3A was <1 Å, suggesting that the docking calculations method was reliable for the calculations of the docking poses of Jun571. The highest score-docking poses of Jun571 inside the three 2C proteins were used for the MD simulations to investigate the binding profile of Jun571. The three complexes consist of ~207 amino acid residues and ~3183 atoms. The docking pose of Jun6504 in EV-D68 2C was generated as described above using the Schrödinger Glide extra precision. The Glide XP GScore was −7.703.

MD simulations. MD simulations were carried to the complexes of Jun571 and Jun6504 with CVB3 2C, EV-A71 2C, and EV-D68 2C proteins with docking poses prepared as described previously. Each complex was solvated using the TIP3P water model[40]. Using the "System Builder utility of Desmond v4.9 (Schrödinger Release 2021-1: Desmond Molecular Dynamics System, D. E. Shaw Research, New York, NY, 2021. Maestro-Desmond Interoperability Tools, Schrödinger, New York, NY, 2021) each complex was embedded in an orthorhombic water box extending beyond the solute 12 Å in x,y,z direction leading to ~10,000 waters. Sodium and chloride ions were added randomly in the water phase to neutralize the systems and reach the experimental salt concentration of 0.150 M NaCl. The total number of atoms was ~33,000.

The ff19sb force field was used to model all protein and ligand interactions and lipids[40]. The particle mesh Ewald method (PME) was employed to calculate long-range electrostatic interactions with a grid spacing of 0.8 Å[41,42]. Van der Waals and short-range electrostatic interactions were smoothly truncated at 9.0 Å. The Langevin thermostat[43] was utilized to maintain a constant temperature in all simulations, and the Berendsen barostat[44] was used to control the pressure. Periodic boundary conditions were applied $(75 \times 65 \times 74)$ Å^3. The equations of motion were integrated using the multistep RESPA integrator[45] with an inner time step of 2 fs for bonded interactions and non-bonded interactions within a cutoff of 9 Å. An outer time step of 6.0 fs was used for non-bonded interactions beyond the cut-off. Each system was equilibrated in MD simulations with a default protocol for water-soluble proteins provided in Desmond, which consists of a series of restrained MD simulations designed to relax the system, while not deviating substantially from the initial coordinates.

The first simulation was Brownian dynamics run for 100 ps at a temperature of 10 K in the NVT (constant number of particles, volume, and temperature) ensemble with solute heavy atoms restrained with a force constant of 50 kcal mol Å^{-2}. The Langevin thermostat was applied in the NVT ensemble and an MD simulation for 12 ps with solute heavy atoms restrained with a force constant of 50 kcal mol Å^{-2}. The velocities were randomized and MD simulation for 12 ps was performed in the NPT (constant number of particles, pressure, and temperature) ensemble and a Berendsen barostat with solute heavy atoms equally restrained at 10 K and another one at 300 K. The velocities were again randomized and unrestrained MD simulation for 24 ps was performed in the NPT ensemble. The above-mentioned equilibration was followed by a 500 ns simulation without restrains. The simulations were performed on a workstation with a GTX 970. The visualization of the produced trajectories and structures was performed using Maestro or programs Chimera and VMD. Within the 500-ns-MD simulation time, the RMSD of the protein backbone Cα atoms reached a plateau, and the systems were considered equilibrated and suitable for statistical analysis (see Figs. 1d, 5g, j and Supplementary Fig. 2f, 3f).

The visualization of the trajectories was performed using the graphical user interface (GUI) of Maestro, and the protein–ligand interaction analysis was done with the simulation interaction diagram (SID) tool, available with the Desmond v4.9 program. For hydrogen bonding interactions, a distance between donor and acceptor heavy atoms ≤2.5 Å, an angle ≥120° between donor-hydrogen-acceptor atoms and ≥90° between hydrogen-acceptor-bonded atoms were applied. Non-specific hydrophobic contacts were identified when the side chain of a hydrophobic residue fell within 3.6 Å from a ligand's aromatic or aliphatic carbon, while π−π interactions were characterized by stacking of two aromatic groups face-to-face or face-to-edge. Water-mediated hydrogen bonding interactions were characterized by ≤2.7 Å distance between donor and acceptor atoms, as well as an angle ≥110° between donor-hydrogen-acceptor atoms and ≥80° between hydrogen-acceptor-bonded atoms were applied.

Alchemical binding free energies calculations
TI/MD method's principle. The TI/MD method has been described[46]. Free energy is a state function, and thus the free energy difference between states is independent of the path that connects them. To compare ligand binding for two protein mutants 0 and 1, the calculation of $\Delta A_{b,1}$ and $\Delta A_{b,0}$, respectively, is needed and then the difference

$\Delta\Delta A_{b,0\to1}$ (b) or $\Delta\Delta A_{b,0,1}$ (b). The calculation of ΔA_1(b) and ΔA_0(b) is demanded because it includes large changes between the two states. Thus, the calculation of the relative binding free energies for **Jun571** and **Jun6504** bound to EV-D68 2C WT and D183V mutant protein or **Jun6504** bound to EV-D68 2C WT and P190L mutant protein can be performed instead using the MBAR method[47] and applying a thermodynamic cycle listed below, i.e., using the ΔG values obtained for the transformations of the proteins in the bound (b) and the solvent (s; water) state, $\Delta G_{b,0,1}$ and $\Delta G_{s,0,1}$(s), respectively, according to equation (Supplementary Fig. 9).

Briefly, a thermodynamic parameter λ that smoothly connects states 0 and 1 through a λ-dependent potential $U(r^N; \lambda)$, such that $U(r^N; 0) = U_0(r^N)$ and $U(r^N; 1) = U_1(r^N)$. The transformation is broken down into a series of M steps corresponding to a set of λ values $\lambda_1, \lambda_2,..., \lambda_M$ ranging from 0 to 1, such that there is sufficient phase space overlap between neighboring intermediate λ states. The TI estimator computes the free energy change of transformation $0 \to 1$ by integrating the Boltzmann averaged $dU(\lambda)/d\lambda$ as is described in Eq. (1)

$$
\begin{aligned}
\Delta A_{0\to1} &= \int_0^1 d\lambda \left\langle \frac{dU(r^N; \lambda)}{d\lambda} \right\rangle_\lambda \\
&= \Delta A_{0\to1} \approx \sum_{k=1}^{M} w_k \left\langle \frac{dU(r^N; \lambda)}{d\lambda} \right\rangle_{\lambda_k}
\end{aligned}
\tag{1}
$$

where the second sum indicates numerical integration over M quadrature points (λ_k, for $k = 1,..., M$) with associated weights w_k. A linear extrapolation between states can be applied for the construction of $U_1(r^N; \lambda)$, while with Amber18 softcore potentials[48–50] the Lennard-Jones and Coulomb term potentials are described according to Eq. (2)

$$
\begin{aligned}
U(r^N; \lambda) &= U_0^{SC}(r^N; \lambda) + \lambda \Delta U^{SC}(r^N; \lambda) \\
&= U_0^{SC}(r^N; \lambda) + \lambda \left(U_1^{SC}(r^N; 1-\lambda) - U_0^{SC}(r^N; \lambda) \right)
\end{aligned}
\tag{2}
$$

MBAR[47] calculates the free energy difference between neighboring intermediate states using Eq. (3)

$$
\Delta A_{\lambda\to\lambda+1} = -\ln\ln \frac{\langle w\exp(-\beta U_{\lambda+1}) \rangle_\lambda}{\langle w\exp(-\beta U_{\lambda+1}) \rangle_{\lambda+1}}
\tag{3}
$$

where w is a function of $A(\lambda)$ and $A(\lambda+1)$. The equation is solved iteratively to give the free energy change of neighboring states $\Delta A(\lambda \to \lambda+1)$, which, via combination, yields the overall free energy change. The MBAR method has been shown to minimize the variance in the calculated free energies, by making more efficient use of the simulation data[47,51–53].

TI/MD calculations protocol

For the TI/MD calculations, the experimental structure of the protein–ligand with the solvent around, was used as starting structure for the alchemical transformations between amino acids. For the ligand their protonated form assumed at pH 8 was used.

Setups were performed by using the Amber22 software[54,55]. To start the process, we extracted the protein and ligand from the solvent box into a new PDB file. Then, by initializing the pdb4amber module we mutated the necessary amino acid to create a new PDB file for each protein mutation. Afterward, we processed the mutant and non-mutant protein–ligand PDB files to extract the protein-only into a new PDB file. By using the tleap module of Amber22, we merged the protein–ligand and protein only PDB files (mutants and non-mutant) into a prmtop file (now the prmtop file has both protein and protein-mutant or complex and complex mutant). Then, by using the parmed module and the tiMerge command, we were able to merge these two different proteins (mutant and non-mutant) into one copy of the duplicated protein, and the mutated residue was correctly linked to

the protein. For the protein, we used the ff19sb[40], for the ligand we used GAFF2, for the water and ions we used the tip3p model[56].

The initial geometries were minimized using 20,000 steps of steepest descent minimization at $\lambda = 0.5$. These minimized geometries were used for simulations at all λ values. Eleven λ values were applied, equally spaced between 0.0 and 1.0. In each MD simulation the system was heated to 298 K for 500 ps using the Langevin[43] thermostat (dynamics) for temperature control, as implemented in Amber22 software, employing a Langevin collision frequency of $2.0\,\text{ps}^{-1}$ in the presence of harmonic restraint with force constant $10\,\text{kcal}\,\text{mol}^{-1}\,\text{Å}^{-2}$ on all membrane, protein, and ligand atoms. The Berendsen barostat[57] was used to adjust the density over the 500 ps of equilibration at constant pressure (NPTγ) simulation using $\gamma = 10\,\text{dyn}\,\text{cm}^{-1}$ with a target pressure of 1 bar and a 2 ps coupling time. Then, a 500 ps of NVT equilibration MD simulation was applied following by 2 ns NVT production MD simulation without restraints. Energies were recorded every 1 ps, and coordinates were saved every 10 ps. Production simulations recalculated the potential energy at each λ value every 1 ps for later analysis with MBAR[47,51].

The bond constraint SHAKE algorithm[58] was disabled for the TI calculations performed with Amber GPU-TI module pmemdGTI[59,60], and therefore a time step of 1 fs was used for all MD simulations. Long range electrostatics were calculated using the PME method[41,42] with a 1 Å grid, and short-range non-bonding interactions were truncated at 12 Å with a continuum model long range correction applied for energy and pressure.

For each alchemical calculation, dual topology was applied, that does not convert one species to another, but only converts between dummy atoms and an interacting species, but usually uses softcore potentials. The one-step protocol was applied, where in the softcore potential, the electrostatic and van der Waals interactions are scaled simultaneously.

The final states 0 and 1 of the alchemical calculations $0 \to 1$ or $1 \to 0$, complexes as resulted from the alchemical transformations were compared with these complexes structure resulted from the converged 500-ns-MD simulations. This was performed to certify that the 2 ns-MD simulation for each λ-state during the alchemical calculations was enough for the complexes to converge to the same structure with 500 ns-MD simulations. Two repeats of the TI/MD calculation for each alchemical transformation were performed, and the mean values were computed.

Cell lines and viruses

Rhabdomyosarcoma (RD, CCL-136), Vero C1008 (CRL-1586), HeLa (CCL-2), and HEK293T (CRL-3216) cell lines were obtained from the American Type Culture Collection (ATCC) and maintained in Dulbecco's Modified Eagle Medium (DMEM) supplemented with 10% fetal bovine serum (FBS) and 1% penicillin-streptomycin. Cells were cultured at 37 °C in a humidified incubator with 5% CO_2 and routinely screened to confirm the absence of mycoplasma contamination.

Enterovirus D68 (EV-D68) strains US/MO/14-18947, US/KY/14-18953, US/MO/14-18949, US/IL/14-18952, and US/IL/14-18956 (ATCC); Coxsackievirus B3 (CVB3) Nancy strain (VR-30); Enterovirus A71 (EV-A71) Tainan/4643/1998 (BEI Resources, NR-471); Coxsackievirus A6 (CVA6, VR-1801); and human rhinovirus 16 (RV16, VR-283) were sourced from ATCC or BEI Resources. Coxsackievirus A16 (CVA16) and poliovirus type 1 were provided by Dr. William Nix (CDC) under a material transfer agreement. Viral stocks were propagated in RD cells (EV-D68, EV-A71, CVA6, CVA16), Vero C1008 cells (CVB3), or HeLa cells (RV16, poliovirus type 1) prior to use in infection assays.

Antiviral assays

Cytopathic effect (CPE) assay and plaque assay were developed for multiple viruses in our laboratory and routinely employed to evaluate the antiviral activity of compounds in cell culture[61]. For the CPE assay,

cell lines were selected based on viral tropism: RD cells were used for EV-D68, EV-A71, CVA6, and CVA16; HeLa cells for poliovirus type 1 and RV16; and Vero cells for CVB3. Cells were seeded into 96-well plates to reach approximately 90% confluency after 24 h. Prior to infection, the culture medium was removed, and cells were washed with $1 \times$ PBS. Virus inoculum prepared in infection media at the desired multiplicity of infection (MOI) was added (100 μL per well), followed by a 1–2 h incubation for viral adsorption. Next, 100 μL of infection media containing the test compound at the indicated concentrations (without virus) was added to each well. Upon full CPE development (typically within 2–3 days), media were aspirated and replaced with neutral red solution (50 μg/mL) to stain viable cells. Absorbance was read at 540 nm using a Multiskan FC Microplate Photometer (Thermo Fisher Scientific), and EC_{50} values were calculated by plotting absorbance against log compound concentration using non-linear regression in GraphPad Prism 8.

Plaque reduction assay for EV-D68 was performed as previously described[62,63]. RD cells were seeded in six-well plates and cultured to >95% confluency within 24 h. Prior to infection, cells were washed with $1 \times$ PBS supplemented with magnesium and calcium. Each well was then infected with 500 μL of EV-D68-containing infection media, yielding approximately 100–120 plaque-forming units (PFU) per well. Following a 1–2 h incubation at 33 °C to allow viral attachment, the inoculum was removed, and cells were overlaid with 4 mL of DMEM containing 2% FBS, 30 mM MgCl₂, 1.2% Avicel (FMC BioPolymer), and the indicated concentration of Jun6504. Plates were incubated at 33 °C in a 5% CO_2 atmosphere for 3 days. After incubation, the Avicel overlay was removed, and cells were stained with crystal violet. Plaque areas were quantified using ImageJ software, and EC_{50} values were calculated by plotting plaque area against the log concentration of **Jun6504** using non-linear regression in GraphPad Prism 8[64].

Virus plaque purification
The plaque purification procedure was adapted from the standard plaque reduction assay. Prior to purification, the viral stock from passage 10 was titrated by plaque assay. RD cells were seeded in six-well plates and incubated overnight at 37 °C to achieve over 95% confluence. Based on the titration results, the virus stock was diluted to the desired concentrations using viral diluent consisting of DMEM supplemented with 2% FBS, 1% penicillin-streptomycin (P/S), and 30 mM MgCl₂. A total of 500 μL of the diluted virus was added to each well, followed by gentle swirling to ensure even distribution. Plates were incubated at 33 °C for 1 h to allow virus adsorption.

Meanwhile, a 0.75% agarose overlay medium was prepared by mixing equal volumes of 1.5% autoclaved agarose (A9539, Sigma, maintained at 50 °C) with 2× DMEM supplemented with 4% FBS, 2% P/S, and 60 mM MgCl₂. After confirming the appropriate temperature, 2 mL of overlay medium was gently added to each well. Plates were left at room temperature for 10 min to allow the overlay to solidify, then incubated at 33 °C for 60 h.

Clear and countable plaques were visible to the naked eye. Twelve well-isolated plaques were selected and marked on the bottom of the plates. Using sterile glass pipette tips, plaques were picked along with topping agarose and transferred into sterile centrifuge tubes containing 500 μL of viral diluent. Tubes were rotated overnight at 4 °C to facilitate viral release, and the recovered viruses were subsequently amplified by inoculation into fresh RD cell monolayers in six-well plates.

Cytotoxicity assay
The cytotoxicity of 2C inhibitors in RD, Vero C1008, and HeLa cells was assessed using the neutral red uptake assay, following previously established protocols[65,66]. Cells were seeded in 96-well plates to reach over 95% confluency after 24 h. The growth medium was then removed, and cells were washed with 1× PBS. Subsequently, 200 μL of

DMEM supplemented with 2% FBS and serial dilutions of the 2C inhibitors was added to each well. Incubation times matched those used in the corresponding CPE assays. After incubation, viable cells were stained with neutral red dye (50 μg/mL), and CC_{50} values were calculated by plotting absorbance against the log concentration of each compound using non-linear regression in GraphPad Prism 8.

Differential scanning fluorimetry (DSF)
The binding of **Jun6504** to EV-A71 Tainan/4643/1998, EV-D68 US/MO/14-18947, CVB3 Nancy 2C wildtype, or mutant 2C proteins was assessed using DSF with a Thermal Fisher QuantStudio™ 5 RealTime PCR System as previously described[35]. Briefly, **Jun6504** was incubated at concentrations of 0, 3, 10, 30, 100, and 300 μM with 4 μM of either wild-type or mutant 2C protein at 37 °C for 1 h. After incubation, SYPRO Orange dye (Thermo Fisher) was added, and fluorescence was monitored under a temperature gradient from 30 to 90 °C, increasing at a rate of 0.05 °C per second. Melting temperatures (Tm) were determined using Protein Thermal Shift Software v1.3. ΔT_m values were calculated by subtracting the Tm of the DMSO control from the Tm observed in the presence of **Jun6504**.

Serial passage experiment
To identify mutations induced by **Jun6504**, serial passage experiments of EV-D68 were conducted, followed by sequencing as previously described[31,63]. Subsequently, EV-D68 recombinant viruses harboring 2C mutations identified in the serial passage experiment were generated using reverse genetics. The detailed procedure can be found in ref. 31.

Time of addition experiment
A time-of-addition experiment was conducted as previously described[67,68]. Briefly, RD cells were infected by EV-D68 US/MO/14−18947 at an MOI of 0.2. 3 μM of Jun6-50-4 was added at different time points before, during, or after viral infection. Viruses were harvested from the cell culture supernatant at 14 h post-infection, and the viral titers were quantified by plaque assay.

Compound synthesis and characterization
Details for the synthesis procedure and compound characterizations (HNMR, CNMR, MS) can be found in the Supplementary Material.

In vivo PK profiling in BALB/c mice of 2C inhibitors
The in vivo PK studies in BALB/c mice were carried out in accordance with the protocol approved by the Institutional Animal Care and Use Committee of the University of Arizona (Protocol # 17-355).

Acetonitrile, methanol, and water (LC−MS grade) were purchased from Fisher Scientific (Fair Lawn, NJ, USA). Formic acid was purchased from Sigma-Aldrich (St. Louis, MO).

Plasma samples (5 μl each) were mixed with 45 μL of methanol and 10 μL of internal standard (IS; UAWJ102 100 ng/mL in methanol). The mixture was vortexed for 30 s, centrifuged at 15,000 rpm for 5 min, then the supernatant was diluted with 900 μl Milli Q water and loaded onto OASIS® HLB cartridge (C18, 1 mL/30 mg, Waters Corporation, Milford, MA) pre-conditioned with 1 mL methanol followed by 1 mL water, and the cartridge was then washed with 1 mL water. The analytes were finally eluted from the cartridges with 1 mL of methanol for HPLC-MS/MS analysis.

Jun5532, **Jun10241**, **Jun6504**, **Jun9351**, and **Jun6962** were detected using LC−MS/MS. The LC−MS system consisted of an Agilent 1290 UPLC system (Agilent Technologies, Santa Clara, CA) and a Sciex Qtrap6500⁺ Mass Spectrometer (AB SCIEX, Framingham, MA). Analytes were separated on an EclipsePlus C18 column (2.1 × 50 mm, 1.8 μm, Agilent) at a temperature of 35 °C. Compound **Jun5532**, **Jun6504**, **Jun9351**, and **Jun6962** were eluted with mobile phase containing 0.1% formic acid (v/v) in water and mobile phase B containing

0.1% formic acid (v/v) in methanol, at a flow rate of 0.3 mL/min as follows: 10% B (0–0.2 min), 10% B → 95% B (0.2–5 min), 95% B (5–7 min), 95% B → 10% B (7–7.1 min), 10% B (7.1–10 min). Compound **Jun10241** was eluted with mobile phase containing 0.1% formic acid (v/v) in water and mobile phase B containing 0.1% formic acid (v/v) in acetonitrile, also at a flow rate of 0.3 mL/min as follows: 10% B (0–0.5 min), 10% B → 95% B (0.5–0.6 min), 95% B (0.6–7 min), 95% B → 10% B (7–7.1 min), 10% B (7.1–10 min). The MS was operated in the positive ion mode, using electrospray ionization. The ion spray voltage and temperature were set at 5000 V and 500 °C, respectively. Curtain gas, ion source gas1 and ion source gas2 were set at 40, 40, and 10 psi, respectively. **Jun5532**, **Jun10241**, **Jun6504**, **Jun9351**, **Jun6962**, and the internal standard (IS, UAWJ102) were detected using multiple reaction monitoring (MRM), with a dwell time of 200 msec per transition, at m/z 290.2/231.1, 292.0/275.2, 328.1/299.1, 302.1/243.1, 314.2/228.2 and 289.1/139.1, respectively. Retention times for **Jun5532**, **Jun6504**, **Jun9351**, **Jun6962** and the IS were 4.80, 4.72, 4.52, 6.54, and 3.18 min, respectively. Retention for **Jun10241** and the IS were 2.00 and 2.10 min, respectively. For quantitative analysis of **Jun5532**, **Jun10241**, **Jun6504**, **Jun9351**, and **Jun6962**, pure compounds (20 to 4000 ng/mL in 5 µl methanol), along with 10 µL IS (at 100 ng/ml in methanol), were added to 5 µL of blank mouse plasma to construct the calibration curve.

The pharmacokinetic parameters were calculated using PK solver (Microsoft, Redmond, WA) by assuming a noncompartmental model.

In vivo EV-D68 infection mouse model study
For the EV-D68 infection mouse model studies in Swiss Webster mice, the experiments were carried out in accordance with the protocol approved by the Institutional Animal Care and Use Committee of the University of Colorado (Protocol # 00075).

Treatment model. Litter size was kept constant between 9 and 11 animals per dam by mixing litters of the same age. Postnatal day 2 (P2) Swiss Webster mice were intramuscularly (IM) injected with 10 µL of EV-D68 at 10,000x TCID$_{50}$/pup into the left quadriceps muscle. An equal number of males and females were used in these experiments, and no statistically significant sex effects were observed. Animals were infected with EV-D68 isolate US/IL/14−18952, which was purchased from BEI resources NR-49131 LOT#63205985. Drug treatment was initiated within 30 min following IM viral infection (in the immediate treatment model) or at 24 h post-IM infection (in the 24-h delayed treatment model), and treatment was repeated once daily for the remainder of the experiment. The drug was dissolved in 10% DMSO and mixed with 90% corn oil immediately prior to intraperitoneal injection at a concentration of 50 mg/kg (25 µL total injection volume per pup). "No drug" treated controls were dosed intraperitoneally with 25 µL of 90% corn oil + 10% DMSO. Pups were checked once daily to record paralysis scores and weight for each animal. Pups were housed with dams until the time of weaning (P21) in a BSL2 facility kept at 23 °C, 43% relative humidity, and kept on a 12- to-12-h light-dark cycle with ad libitum access to food and water.

Paralysis scoring scale. Paralysis scores were assessed as previously published by ref. 21, with the exception that in rare instances, a score of 1.5 or 2.5 was used to better capture limb paralysis that was borderline between bins. Briefly, each limb was scored from 0 to 3, where 0 represents normal limb movement and 3 represents a complete loss of function in the limb. The score from each limb was added together to give a total paralysis score up to 12 for a completely paralyzed, quadriplegic animal. An animal was sacked if its paralysis score was ≥11 or if its weight dropped below 60% of the litter average.

TCID$_{50}$ protocol. Rhabdomyosarcoma cells (ATCC CCL-136) were plated at 3000 cells/well into two sets of five columns in a 96-well flat-bottomed cell culture plate. After 24 h, serial tenfold dilutions of EV-D68 were added to the appropriate wells and incubated at 33 °C for 7 days. All wells were examined for signs of cytopathic effect, and TCID$_{50}$ (50% tissue culture infectious dose) values were calculated using the Reed-Muench method. All TCID$_{50}$ values in this paper represent TCID$_{50}$/mL even if it is not explicitly stated.

Determination of drug concentration in the spinal cord by LC–MS/MS. Swiss Webster mouse pups were intraperitoneally injected with Jun6-50-4 (at 50 mg/kg) beginning on postnatal day 2 and continuing daily for 7 days. The final dose of Jun6-50-4 was given 1 h prior to harvesting spinal cord tissue. The spinal column was cut at C2 and L3, then pressurized, and ice-cold PBS was used to force the spinal cord from the spinal column. Spinal cords were weighed, frozen, and then homogenized in 10 x volumes (v/w, i.e., 1 mg tissue added 10 µL buffer) of PBS buffer (137 mM NaCl, 2.7 mM KCl, 10 mM Na$_2$HPO$_4$, and 1.8 mM KH$_2$PO$_4$ pH = 7.2) using NEXT ADVANCE Bullet Blender (speed setting at 10'; 3 × 5 min with 5 min rest on ice between the cycle). The Jun6-50-4 was extracted by mixing 20 µL of each homogenate with 10 µL internal standard (IS; Jun6-50-4, 1 µg/mL) and 100 µL methanol. Then the mixture was vortexed for 30 s at room temperature (RT) and centrifuged at 15,000 rpm for 5 min at 4 °C. The supernatant (100 µL) was processed for LC–MS/MS analysis in the same way as for the plasma, as described above. The eluates of 2 µL from the OASIS® HLB cartridge were injected for LC–MS/MS analysis. Jun6-50-4 in tissue lysate was detected using the same LC–MS/MS system as described in PK analysis above. The analytes were separated on an EclipsePlus C18 column (2.1 × 50 mm, 1.8 µm, Agilent) at a temperature of 35 °C, with mobile phase A containing 0.1% formic acid (v/v) in water and mobile phase B containing 0.1% formic acid (v/v) in methanol. Gradient elution was applied at a flow rate of 0.2 mL/min. The MS was operated in the positive ion mode, using electrospray ionization. The ion spray voltage and temperature were set at 5500 V and 500 °C, respectively. Curtain gas, ion source gas1 and ion source gas 2 were set at 40, 50, and 50 psi, respectively. Tissue extract and the internal standard were detected using multiple reaction monitoring (MRM), with a dwell time of 200 msec per transition, at m/z 328.1/299.1 and 289.1/139.1, respectively. For quantitative analysis of Jun6-50-4 in tissue lysate, 10 µL standards (10 to 10,000 ng/mL in methanol), along with 10 µL of internal standard (at 1 µg/mL in methanol), were added to 20 µL of blank plasma to construct the calibration curve.

IHC protocol. Spinal cord tissue was taken from Swiss Webster pups, in the 24-h delayed treatment model, at 6 days post-infection. Spinal cords were placed in 4% paraformaldehyde for 24 h, briefly rinsed in PBS, and then soaked in 30% sucrose for 48 h. Tissue was then frozen in OCT, and the lumbar enlargement was sectioned at 20 µm using a cryotome. Standard IHC protocol for fresh frozen tissue was followed. Antigen retrieval was performed for 30 min using 10 mM Citrate buffer at pH 6.0. Sections were blocked in (0.1% triton, 5% NGS, 1% BSA, 0.05% tween20, in PBS) for 1 h, then primary antibodies were added to blocking buffer as follows: anti-NeuN mAb from AbCam (ab279297) used at 1:100; anti-EV-D68 VP2 pAb from GeneTex (GTX132314) used at 1:50; antiChAT mAb from AbCam ([EPR16590] ab178850) used at 1:50. Samples were incubated in primary antibody for 24-h at room temperature. Nuclear stain was Hoechst 33342, trihydrochloride used at 1 ug/mL.

Statistical analysis. JMP®, Version 15.0.0. SAS Institute Inc., Cary, NC, 1989−2007, was used for all statistical calculations. We did not observe sex differences in survival or paralysis for any experiment. We did observe litter effects, so pups were mixed between litters (whenever possible), and all litters included a 50/50 mix of treated and control animals. A total of 20 animals in the immediate treatment model and 35 animals in the 24-h delayed treatment model (from 6 litters) were

used for these experiments. Three animals in the control group of the 24 h delayed treatment model were sacked before the completion of the experiment (days 8, 9, and 11), so their last recorded paralysis score (12, 11, and 11, respectively) was carried forward to the end of the experiment.

Reporting summary

Further information on research design is available in the Nature Portfolio Reporting Summary linked to this article.

Data availability

All data generated or analyzed in this study are included in the main text and the supplementary information files. Publicly available datasets used in this study are X-ray crystal structures of CVB3 2C with (S)-fluoxetine (PDB ID 6S3A), the apo structure of EV-A71 2C (PDB ID 5GQ1), and EV-A71 2C with ATPγS (PDB: 5GRB). The following link is provided to access the initial and final configurations of the following complexes in MD simulations: **Jun571** + EV-D68 2C, **Jun571** + EV-A71 2C, **Jun571** + CVB3 2C, **Jun6504** + EV-D68 2C, **Jun6504** + EV-D68 2C-D183V, and **Jun6504** + EV-D68 2C_F190L: https://github.com/georgioukyriakos/enterovirus_d68. Source data are provided with this paper.

References

1. Baggen, J., Thibaut, H. J., Strating, J. & van Kuppeveld, F. J. M. The life cycle of non-polio enteroviruses and how to target it. *Nat. Rev. Microbiol.* **16**, 368–381 (2018).
2. Schieble, J. H., Fox, V. L. & Lennette, E. H. A probable new human picornavirus associated with respiratory diseases. *Am. J. Epidemiol.* **85**, 297–310 (1967).
3. Khetsuriani, N. et al. Enterovirus surveillance-United States, 1970-2005. *MMWR Surveill. Summ.* **55**, 1–20 (2006).
4. Midgley, C. M. et al. Severe respiratory illness associated with a nationwide outbreak of enterovirus D68 in the USA (2014): a descriptive epidemiological investigation. *Lancet Respir. Med.* **3**, 879–887 (2015).
5. Midgley, C. M. et al. Severe respiratory illness associated with enterovirus D68 - Missouri and Illinois, 2014. *MMWR Morb. Mortal. Wkly. Rep.* **63**, 798–799 (2014).
6. Messacar, K., Pretty, K., Reno, S. & Dominguez, S. R. Continued biennial circulation of enterovirus D68 in Colorado. *J. Clin. Virol.* **113**, 24–26 (2019).
7. Benschop, K. S. et al. Re-emergence of enterovirus D68 in Europe after easing the COVID-19 lockdown, September 2021. *Eur. Surveill.* **26**, 2100998 (2021).
8. Ma, K. C. et al. Increase in acute respiratory illnesses among children and adolescents associated with rhinoviruses and enteroviruses, including enterovirus D68 - United States, July-September 2022. *MMWR Morb. Mortal. Wkly. Rep.* **71**, 1265–1270 (2022).
9. Hu, Y., Musharrafieh, R., Zheng, M. & Wang, J. Enterovirus D68 antivirals: past, present, and future. *ACS Infect. Dis.* **6**, 1572–1586 (2020).
10. Rhoden, E., Zhang, M., Nix, W. A. & Oberste, M. S. In vitro efficacy of antiviral compounds against enterovirus D68. *Antimicrob. Agents Chemother.* **59**, 7779–7781 (2015).
11. Sun, L. et al. Antiviral activity of broad-spectrum and enterovirus-specific inhibitors against clinical isolates of enterovirus D68. *Antimicrob. Agents Chemother.* **59**, 7782–7785 (2015).
12. Musharrafieh, R. et al. Validating enterovirus D68-2A(pro) as an antiviral drug target and the discovery of telaprevir as a potent D68-2A(pro) inhibitor. *J. Virol.* **93**, e02221–02218 (2019).
13. Liu, Y. et al. Structure and inhibition of EV-D68, a virus that causes respiratory illness in children. *Science* **347**, 71–74 (2015).
14. Hurst, B. L., Evans, W. J., Smee, D. F., Van Wettere, A. J. & Tarbet, E. B. Evaluation of antiviral therapies in respiratory and neurological disease models of enterovirus D68 infection in mice. *Virology* **526**, 146–154 (2019).
15. Ulferts, R. et al. Selective serotonin reuptake inhibitor fluoxetine inhibits replication of human enteroviruses B and D by targeting viral protein 2C. *Antimicrob. Agents Chemother.* **57**, 1952–1956 (2013).
16. Hurdiss, D. L. et al. Fluoxetine targets an allosteric site in the enterovirus 2C AAA+ ATPase and stabilizes a ring-shaped hexameric complex. *Sci. Adv.* **8**, eabj7615 (2022).
17. Bauer, L. et al. Fluoxetine inhibits enterovirus replication by targeting the viral 2C protein in a stereospecific manner. *ACS Infect. Dis.* **5**, 1609–1623 (2019).
18. Musharrafieh, R. et al. Discovery of quinoline analogues as potent antivirals against enterovirus D68 (EV-D68). *J. Med. Chem.* **62**, 4074–4090 (2019).
19. Musharrafieh, R., Kitamura, N., Hu, Y. & Wang, J. Development of broad-spectrum enterovirus antivirals based on quinoline scaffold. *Bioorg. Chem.* **101**, 103981 (2020).
20. Smee, D. F., Evans, W. J., Nicolaou, K. C., Tarbet, E. B. & Day, C. W. Susceptibilities of enterovirus D68, enterovirus 71, and rhinovirus 87 strains to various antiviral compounds. *Antivir. Res.* **131**, 61–65 (2016).
21. Hixon, A. M., Clarke, P. & Tyler, K. L. Evaluating treatment efficacy in a mouse model of enterovirus D68-associated paralytic myelitis. *J. Infect. Dis.* **216**, 1245–1253 (2017).
22. Messacar, K. et al. Safety, tolerability, and efficacy of fluoxetine as an antiviral for acute flaccid myelitis. *Neurology* **92**, e2118–e2126 (2019).
23. Frost, J. et al. Telaprevir treatment reduces paralysis in a mouse model of enterovirus D68 acute flaccid myelitis. *J. Virol.* **97**, e0015623 (2023).
24. Lane, T. R. et al. Efficacy of an isoxazole-3-carboxamide analog of pleconaril in mouse models of enterovirus-D68 and Coxsackie B5. *Antivir. Res.* **216**, 105654 (2023).
25. Wang, S. H., Wang, K., Zhao, K., Hua, S. C. & Du, J. The structure, function, and mechanisms of action of enterovirus non-structural protein 2C. *Front. Microbiol.* **11**, 615965 (2020).
26. Yeager, C. et al. Enteroviral 2C protein is an RNA-stimulated ATPase and uses a two-step mechanism for binding to RNA and ATP. *Nucleic Acids Res.* **50**, 11775–11798 (2022).
27. Li, J. P. & Baltimore, D. Isolation of poliovirus 2C mutants defective in viral RNA synthesis. *J. Virol.* **62**, 4016–4021 (1988).
28. Wang, C., Jiang, P., Sand, C., Paul, A. V. & Wimmer, E. Alanine scanning of poliovirus 2CATPase reveals new genetic evidence that capsid protein/2CATPase interactions are essential for morphogenesis. *J. Virol.* **86**, 9964–9975 (2012).
29. Wang, J., Hu, Y. & Zheng, M. Enterovirus A71 antivirals: past, present, and future. *Acta Pharm. Sin. B* **12**, 1542–1566 (2022).
30. Bauer, L. et al. Rational design of highly potent broad-spectrum enterovirus inhibitors targeting the nonstructural protein 2C. *PLoS Biol.* **18**, e3000904 (2020).
31. Hu, Y., Kitamura, N., Musharrafieh, R. & Wang, J. Discovery of potent and broad-spectrum pyrazolopyridine-containing antivirals against enteroviruses D68, A71, and coxsackievirus B3 by targeting the viral 2C protein. *J. Med. Chem.* **64**, 8755–8774 (2021).
32. Xing, Y., Zuo, J., Krogstad, P. & Jung, M. E. Synthesis and structure-activity relationship (SAR) studies of novel pyrazolopyridine derivatives as inhibitors of enterovirus eeplication. *J. Med. Chem.* **61**, 1688–1703 (2018).
33. Guan, H. et al. Crystal structure of 2C helicase from enterovirus 71. *Sci. Adv.* **3**, e1602573 (2017).
34. Tran, T. T. V., Tayara, H. & Chong, K. T. Artificial intelligence in drug metabolism and excretion prediction: recent advances, challenges, and future perspectives. *Pharmaceutics* **15**, 1260 (2023).

35. Hu, Y. et al. Naturally occurring mutations of SARS-CoV-2 main protease confer drug resistance to nirmatrelvir. *ACS Cent. Sci.* **9**, 1658–1669 (2023).

36. Niesen, F. H., Berglund, H. & Vedadi, M. The use of differential scanning fluorimetry to detect ligand interactions that promote protein stability. *Nat. Protoc.* **2**, 2212–2221 (2007).

37. Chen, T. C. et al. Novel antiviral agent DTriP-22 targets RNA-dependent RNA polymerase of enterovirus 71. *Antimicrob. Agents Chemother.* **53**, 2740–2747 (2009).

38. Ma, C., Hu, Y., Zhang, J. & Wang, J. Pharmacological characterization of the mechanism of action of R523062, a promising antiviral for enterovirus D68. *ACS Infect. Dis.* **6**, 2260–2270 (2020).

39. Rudy, M. J., Frost, J., Clarke, P. & Tyler, K. L. Neutralizing antibody given after paralysis onset reduces the severity of paralysis compared to non-specific antibody treated controls in a mouse model of EV-D68 associated acute flaccid myelitis. *Antimicrob. Agents Chemother.* **66**, e0022722 (2022).

40. Tian, C. et al. ff19SB: amino-acid-specific protein backbone parameters trained against quantum mechanics energy surfaces in solution. *J. Chem. Theory Comput.* **16**, 528–552 (2020).

41. Darden, T., York, D. & Pedersen, L. Particle mesh Ewald - an N.log(N) method for Ewald sums in large systems. *J. Chem. Phys.* **98**, 10089–10092 (1993).

42. Essmann, U. et al. A smooth particle mesh Ewald method. *J. Chem. Phys.* **103**, 8577–8593 (1995).

43. Izaguirre, J. A., Catarello, D. P., Wozniak, J. M. & Skeel, R. D. Langevin stabilization of molecular dynamics. *J. Chem. Phys.* **114**, 2090–2098 (2001).

44. Feller, S. E., Zhang, Y. H., Pastor, R. W. & Brooks, B. R. Constant-pressure molecular-dynamics simulation - the Langevin piston method. *J. Chem. Phys.* **103**, 4613–4621 (1995).

45. Humphreys, D. D., Friesner, R. A. & Berne, B. J. A multiple-time-step molecular-dynamics algorithm for macromolecules. *J. Phys. Chem.* **98**, 6885–6892 (1994).

46. Kirkwood, J. G. Statistical mechanics of fluid mixtures. *J. Chem. Phys.* **3**, 300–313 (1935).

47. Procacci, P. Multiple Bennett acceptance ratio made easy for replica exchange simulations. *J. Chem. Phys.* **139**, 124105 (2013).

48. Song, L. F. et al. Using AMBER18 for relative free energy calculations. *J. Chem. Inf. Model* **59**, 3128–3135 (2019).

49. Lee, T. S. et al. Alchemical binding free energy calculations in AMBER20: advances and best practices for drug discovery. *J. Chem. Inf. Model* **60**, 5595–5623 (2020).

50. Steinbrecher, T., Joung, I. & Case, D. A. Soft-core potentials in thermodynamic integration: comparing one- and two-step transformations. *J. Comput. Chem.* **32**, 3253–3263 (2011).

51. Shirts, M. R. & Pande, V. S. Comparison of efficiency and bias of free energies computed by exponential averaging, the Bennett acceptance ratio, and thermodynamic integration. *J. Chem. Phys.* **122**, 144107 (2005).

52. Paliwal, H. & Shirts, M. R. A benchmark test set for alchemical free energy transformations and its use to quantify error in common free energy methods. *J. Chem. Theory Comput.* **7**, 4115–4134 (2011).

53. Tan, Z., Gallicchio, E., Lapelosa, M. & Levy, R. M. Theory of binless multi-state free energy estimation with applications to protein-ligand binding. *J. Chem. Phys.* **136**, 144102 (2012).

54. Case, D. A. et al. The Amber biomolecular simulation programs. *J. Comput. Chem.* **26**, 1668–1688 (2005).

55. Case, D. A. et al. AmberTools. *J. Chem. Inf. Model* **63**, 6183–6191 (2023).

56. Jorgensen, W. L., Chandrasekhar, J., Madura, J. D., Impey, R. W. & Klein, M. L. Comparison of simple potential functions for simulating liquid water. *J. Chem. Phys.* **79**, 926–935 (1983).

57. Berendsen, H. J. C., Postma, J. P. M., van Gunsteren, W. F., DiNola, A. & Haak, J. R. Molecular dynamics with coupling to an external bath. *J. Chem. Phys.* **81**, 3684–3690 (1984).

58. Ryckaert, J.-P., Ciccotti, G. & Berendsen, H. J. C. Numerical integration of the cartesian equations of motion of a system with constraints: molecular dynamics of n-alkanes. *J. Comput. Phys.* **23**, 327–341 (1977).

59. He, X. et al. Fast, accurate, and reliable protocols for routine calculations of protein-ligand binding affinities in drug design projects using AMBER GPU-TI with ff14SB/GAFF. *ACS Omega* **5**, 4611–4619 (2020).

60. Lee, T. S., Hu, Y., Sherborne, B., Guo, Z. & York, D. M. Toward fast and accurate binding affinity prediction with pmemdGTI: an efficient implementation of GPU-accelerated thermodynamic integration. *J. Chem. Theory Comput.* **13**, 3077–3084 (2017).

61. Hu, Y., Ma, C. & Wang, J. Cytopathic effect assay and plaque assay to evaluate in vitro activity of antiviral compounds against human coronaviruses 229E, OC43, and NL63. *Bio Protoc.* **12**, e4314 (2022).

62. Hu, Y., Jo, H., DeGrado, W. F. & Wang, J. Brilacidin, a COVID-19 drug candidate, demonstrates broad-spectrum antiviral activity against human coronaviruses OC43, 229E, and NL63 through targeting both the virus and the host cell. *J. Med. Virol.* **94**, 2188–2200 (2022).

63. Ma, C., Hu, Y., Zhang, J., Musharrafieh, R. & Wang, J. A novel capsid binding inhibitor displays potent antiviral activity against enterovirus D68. *ACS Infect. Dis.* **5**, 1952–1962 (2019).

64. Hu, Y., Meng, X., Zhang, F., Xiang, Y. & Wang, J. The in vitro antiviral activity of lactoferrin against common human coronaviruses and SARS-CoV-2 is mediated by targeting the heparan sulfate co-receptor. *Emerg. Microbes Infect.* **10**, 317–330 (2021).

65. Zhang, J. et al. Exploring Ugi-azide four-component reaction products for broad-spectrum influenza antivirals with a high genetic barrier to drug resistance. *Sci. Rep.* **8**, 4653 (2018).

66. Zhang, J. et al. Identification of NMS-873, an allosteric and specific p97 inhibitor, as a broad antiviral against both influenza A and B viruses. *Eur. J. Pharm. Sci.* **133**, 86–94 (2019).

67. Hu, Y. et al. Discovery of dapivirine, a nonnucleoside HIV-1 reverse transcriptase inhibitor, as a broad-spectrum antiviral against both influenza A and B viruses. *Antivir. Res.* **145**, 103–113 (2017).

68. Zhang, J., Hu, Y., Wu, N. & Wang, J. Discovery of influenza polymerase PA-PB1 interaction inhibitors using an in vitro split-luciferase complementation-based assay. *ACS Chem. Biol.* **15**, 74–82 (2020).

69. Hall, J. A simple model for determining affinity from irreversible thermal shifts. *Protein Sci.* **28**, 1880–1887 (2019).

Acknowledgements

Author contributions

K.L., M.J.R., Y.H., and H.T. contributed equally to this work. J.W. and K.L.T. conceived and supervised the research and designed the experiments; J.W. and K.L. designed the inhibitors; K.L. performed chemical syntheses, separation, purification, and structural characterizations; K.L., Y.H., and H.T. performed antiviral assay, cellular cytotoxicity assay, passage experiment, thermal shift assay, and reverse genetics; X.W. and Q.-y.Z. performed the in vivo PK studies; G.L., K.G., and A.K. performed the simulations; M.R. performed in vivo EV-D68 infection mouse model study and the histopathology and immunohistochemistry (IHC) assessment with the assistance of J.F. and C.W.; J.W., K.L., M.J.R., Y.H., H.T., G.L., X.W., P.C., A.K., Q.-y.Z., and K.L.T. analyzed and discussed the data with the assistance of J.F. and C.W.; and J.W., K.L., M.J.R., Y.H., G.L., A.K., and Q.-y.Z. wrote the manuscript with inputs from other co-authors.

Competing interests

Additional information